INSTITUTO
UNIVERSITÁRIO
DE LISBOA

# Short-Axis and Long-Axis Segmentation of Left Ventricle

Alexandre Afonso Rodrigues

Master's in Telecommunications and Computer Engineering

Supervisor:
PhD João Pedro Oliveira,
Associate Professor,
ISCTE - IUL

October, 2024

# Acknowledgment

First I would like to express my gratitude to my supervisor, Professor João Pedro Oliveira. His constant support and patience have all contributed to the successful completion of my thesis.

To my family, words cannot express how grateful I am for their sacrifices, support, and undying trust in me.

My gratitude also goes out to my friends, because their support, understanding, and encouragement have made this trip not just manageable but joyful.

I would like to extend my gratitude to Instituto de Telecomunicações (IT), for their support and providing infrastructural conditions for the development of this thesis.

Finally, thank you to all of the teachers and administrative personnel at ISCTE for creating an academic atmosphere that encourages study and research.

# Resumo

Ainda que, nos últimos anos, tenham existido grandes avanços no que diz respeito a métodos automáticos de segmentação e classificação, os mesmos ainda não são completamente eficazes. Nesta tese apresentamos uma abordagem inovadora para a segmentação do ventrículo esquerdo ao utilizar uma combinação entre dados de ressonâncias magnéticas cardíacas de eixo horizontal e vertical. A metodologia utilizada inclui uma rede neuronal *nnU-Net* pré-treinada que realiza a segmentação de imagens de eixo horizontal, sendo que é integrada com um modelo de contornos ativos para melhorar a precisão da segmentação. Apesar deste tipo de processamento produzir múltiplos resultados para comparação, nós pretendemos realizar uma reconstrução de eixo vertical do ventrículo esquerdo para fornecer uma perspetiva adicional que possa ajudar na compreensão da estrutura anatómica do ventrículo esquerdo. Para alcançar uma representação detalhada no eixo vertical, é necessário realizar um processo de interpolação utilizando os dados recolhidos a partir de diferentes segmentos do eixo horizontal. Ao longo deste trabalho, utilizámos diferentes imagens de vários pacientes provenientes de dois conjuntos de dados distintos: um público e outro privado. Os resultados revelam que a abordagem proposta para melhoria na segmentação do eixo horizontal geralmente aumenta a precisão em determinadas circunstâncias, mantendo a precisão nas restantes, provando, assim, que o *pipeline* proposto se adapta bem a diferentes condições e pode ser útil no diagnóstico de doenças. Demonstramos, ainda, que a combinação de dados entre os vários segmentos de eixo horizontal resulta numa segmentação do ventrículo esquerdo em eixo vertical praticamente acertada.

**Palavras-chave:** Deep Learning, Ventrículo Esquerdo, Ressonância Magnética Cardíaca, Eixo, Segmentação, Reconstrução.

# Abstract

Although there have been major improvements in recent years regarding automatic segmentation and classification approaches, there is still plenty of space for improvement. We present an innovative approach to left ventricle (LV) segmentation using a combination of short-axis and long-axis cardiac magnetic resonance imaging (MRI) data. The methodology used includes a pre-trained nnU-Net neural network to segment short-axis images, which is then integrated with an active contours model to improve the accuracy of segmentation. Despite this kind of processing yields multiple results for comparison, we want to do a long-axis reconstruction of the left ventricle to provide an extra perspective that might help in understanding the anatomical structure of left ventricle. To achieve a detailed long-axis representation we have to do a interpolation process using the collect data from different segmented short-axis slices. Throughout the set of indicated methods, we used different images of several patients from two separate datasets: one public and the other private. Results reveal that presented short-axis segmentation enhancements approach typically improves efficacy for certain circumstances while maintaining accuracy for others, proving that proposed pipeline adapts well to different conditions and may be able to aid in disease diagnosis. We further demonstrate that combining data from several short-axis slices results in a practically accurate long-axis segmentation of the left ventricle.



**Keywords:** Deep Learning, Left Ventricle, Cardiac Magnetic Resonance Imaging, Axis, Segmentation, Reconstruction.

# List of Figures

Figure 1.1 Design Science Research Process Model (taken from [**8**]) 2
Figure 1.2 The Heart's Chambers (taken from [**9**]) 3
Figure 1.3 Acquisition of basal, mid, and apical slices (taken from [**10**]) 4
Figure 1.4 MRI in three different cardiac planes (taken from [**11**]) 5
Figure 1.5 Proposed Pipeline 7

Figure 2.1 Steps of Region of Interest (ROI) detection (taken from [**17**]) 10
Figure 2.2 Generic architecture of convolutional neural network (taken from [**24**]) 13
Figure 2.3 U-Net architecture for LV segmentation (taken from [**25**]) 14
Figure 2.4 RNN Architecture for LV Segmentation (taken from [**27**]) 15
Figure 2.5 GAN architecture for LV segmentation (taken from [**28**]) 16
Figure 2.6 Active Contour Model example. (a) Initialization contours, (b) ground truth, and (c) final segmentation result (taken from [**38**]) 18
Figure 2.7 Radial long-axis reconstruction example (taken from [**41**]) 19

Figure 3.1 ACDC dataset image example 24
Figure 3.2 nnU-Net processes architecture (taken from [**46**]) 26
Figure 3.3 nnU-Net output example (adapted from [**47**]) 27
Figure 3.4 Active contour applied to both shapes (MYO and LV) 30
Figure 3.5 Left Ventricle long-axis reconstruction from short-axis slices (adapted from [**50**]) 31
Figure 3.6 Vertical long-axis view (taken from [**51**]) 32

Figure 4.1 Active contours results for each slice 37
Figure 4.2 Private dataset short-axis image example (left) and its left ventricle segmentation output (right) 39
Figure 4.3 Baseline left ventricle reconstruction example 40
Figure 4.4 Reconstruction points overlaid on long-axis image 41
Figure 4.5 Active contours model results for long-axis segmentation 41
Figure 4.6 Long-axis reconstruction points and their active contours model results 42

# List of Tables

Table 2.1 Number of articles collected per research phase 9

Table 2.2 Segmentation accuracy of the main articles studied and verified on the ACDC dataset 17

Table 4.1 Results obtained for each cross-validation folder 34

Table 4.2 Mean Dice Scores of the segmentation model for each pathological subgroup 35

Table 4.3 Results obtained for different parameters - Basal slice 36

Table 4.4 Results obtained for different parameters - Mid slice 36

Table 4.5 Results obtained for different parameters - Apical slice 37

Table 4.6 Mean segmentation performance of nnU-Net vs the nnU-Net plus active contours 38

# List of Abbreviations

**ACDC:** Automated Cardiac Diagnosis Challenge
**APD:** Average Perpendicular Distance
**AVD:** Absolute Volume Difference
**CMR:** Cardiac Magnetic Resonance Imaging
**CNN:** Convolutional Neural Network
**CT:** Computerized Tomography
**DICOM:** Digital Imaging and Communications in Medicine
**DSC:** Dice Similarity Coefficient
**DSRM:** Design Science Research Process Model
**ED:** Diastolic Phase
**EDV:** End-Diastolic Volume
**EF:** Ejection Fraction
**ES:** Systolic Phase
**ESV:** End-Systolic Volume
**FCNN:** Fully Convolutional Neural Network
**FN:** False Negative
**FP:** False Positive
**GAN:** Generative Adversarial Network
**GLS:** Global Longitudinal Strain
**HD:** Hausdorff Distance
**JSC:** Jaccard Similarity Coefficient
**LAS:** Long-Axis Strain
**LV:** Left Ventricle
**MRI:** Magnetic Resonance Imaging
**MYO:** Myocardium
**RNN:** Recurrent Neural Network
**ROI:** Region of Interest
**RV:** Right Ventricle
**SA:** Short-Axis
**SGD:** Stochastic Gradient Descent
**SPF:** Signed Pressure Force Function
**SSFP:** Steady-State Free Precession
**SV:** Stroke Volumes
**TN:** True Negative

**TP:** True Positive

# Contents

Acknowledgment i

Resumo iii

Abstract v

List of Figures vii

List of Tables ix

List of Abbreviations xi

Chapter 1. Introduction 1
1.1. Motivation and Context 1
1.2. Research Methodology 2
1.2.1. Problem Identification 3
1.2.2. Research Questions 6
1.2.3. Design and Development 6
1.2.4. Thesis organization 7
1.2.5. Contributions 8

Chapter 2. Literature Review 9
2.1. Segmentation 9
2.1.1. Classical Segmentation Methods 10
2.1.2. Evaluation Metrics 10
2.1.3. Deep Learning Segmentation Architectures 12
2.1.4. Segmentation Results Analysis 16
2.2. Active Contour Models 17
2.3. Radial Long-axis Reconstruction and Segmentation 19

Chapter 3. Methodology 23
3.1. Datasets 23
3.1.1. ACDC Dataset 23
3.1.2. Private Dataset 25
3.2. Short-axis Segmentation 25
3.2.1. nnU-Net network 25
3.2.2. Active contours model 28
3.3. Long-axis Segmentation 31

Chapter 4. Results and Discussion 33
4.1. Short-Axis results 33
4.2. nnU-Net plus Active Contours results 35
4.3. Long-axis results 38
4.3.1. Long-axis reconstruction 39
4.3.2. Long-axis segmentation 40

Chapter 5. Conclusions 43
5.1. Conclusion 43
5.2. Future Work 44

References 45

CHAPTER 1

# Introduction

## 1.1. Motivation and Context

There have been major improvements in recent years on many measures of cardiovascular disease, however cardiovascular disease remains the leading cause of death in Europe and is responsible for close to 4.1 million deaths per year [**1**]. Medical imaging plays a vital role in the diagnosis of cardiovascular diseases, particularly Echocardiography, Magnetic Resonances Imaging (MRI) and Computerized Tomography (CT). The interpretation of medical images can be challenging, and there is a need for automated methods to aid in the diagnosis of cardiovascular diseases.

In this work, our focus is on MRI, namely Cardiovascular Magnetic Resonance Imaging (CMR) that is a medical imaging technique that uses a magnetic field and radio waves to produce detailed images of the heart [**2**]. It is a non-invasive and safe method for evaluating the structure and function of the heart and blood vessels. CMR can be used to evaluate a wide range of cardiac conditions and it can also be used to access the left and right ventricle ejection fractions (EF) and stroke volumes (SV), the left ventricle mass and the myocardium thickness [**2**]. However, we can only obtain these values if we perform a segmentation of left (LV) and right (RV) ventricle.

Cardiac image segmentation recognizes several structures within the heart, which can be used to extract measurements and analyze the function of the heart. Cardiac segmentation can be performed manually, but this can be time-consuming and prone to errors. Automated or semi-automated methods have been developed to improve the accuracy and efficiency of cardiac segmentation. These methods use an approach where the Region of Interest (ROI) is user-defined and use techniques such as image processing, pattern recognition, and machine learning to segment the heart structures. Despite the advantages of the automatic cardiac segmentation process, this process faces some challenges, such as limited robustness, lack of user interaction and interpretation of segmentation data.

To solve the automatic cardiac segmentation issues, several international challenges have taken place. Until 2011, we can highlight four articles [**3, 4, 5, 6**] which used efficient techniques that contributed to the significant increase in the robustness and accuracy of the automatic segmentation process. Despite some great improvements were achieved, none had proposed deep learning methods and it was necessary investigate the applicability of their framework to higher quality MRI. In 2015, a new segmentation competition emerged [**7**] that includes the use of deep learning approaches to perform the process of automatic cardiac segmentation. The results obtained showed that the new

deep learning approaches surpassed the techniques previously used and it was seen as a major step forward in the medical computing field.

In this thesis, we pretend to contribute to the field of medical imaging by providing a comprehensive evaluation of the use of deep learning for the left ventricle segmentation using MRI images. The proposed research has the potential to improve the accuracy and efficiency of the diagnosis of left heart diseases, which can ultimately lead to better patient outcomes.

### 1.2. Research Methodology

The research methodology used in this thesis was the Design Science Research Process Model (DSRM) and this research process can be explained by the diagram represented in Figure 1.1.

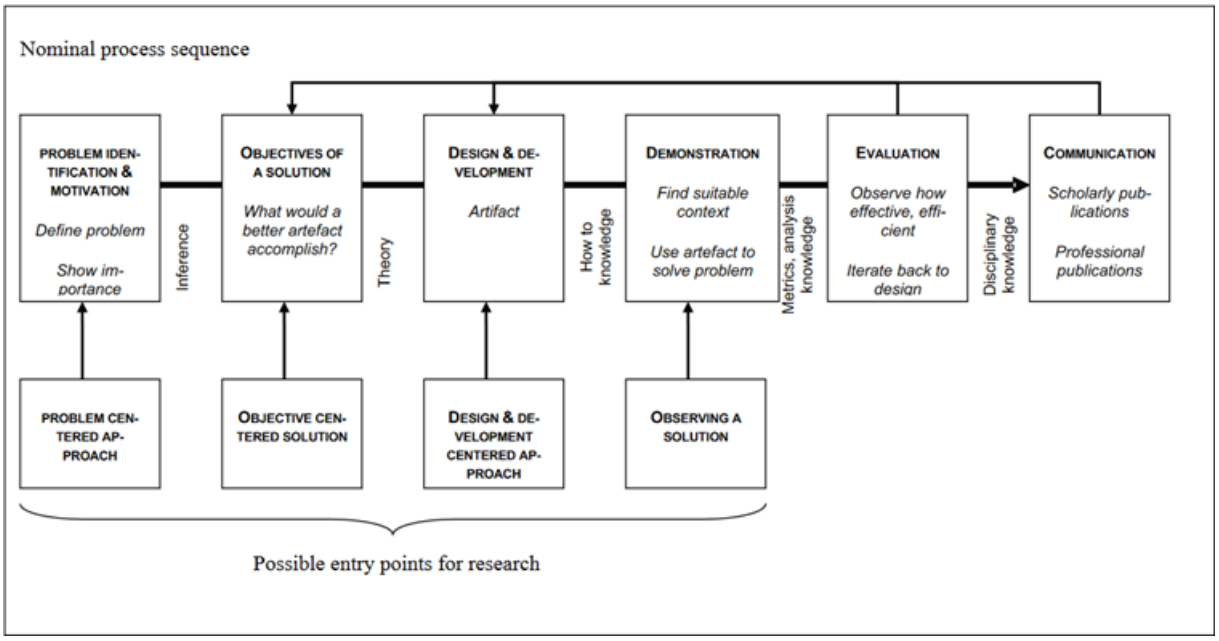



FIGURE 1.1. Design Science Research Process Model (taken from [**8**])

The problem that this dissertation tries to solve has already been previously addressed, so, at the first stage of the research process, it is necessary to realize a problem centered approach. In this approach, we need to identify a specific problem or research question that the model aims to solve. After that, we need to define specific goals or outcomes that the research aims to achieve, and these objectives should be directly related to the previous stage of the research model. The "Design and Development" refers to the process of designing and implementing the solution to the problem or research question identified in the problem identification and motivation step. In addition to these processes, it is necessary to carry out the steps of demonstration, evaluation, and communication. These processes involve showing how the model works and how it can be used to support decision-making, assessing the model's performance, and determining its strengths and weaknesses, and presenting the results of the model and making them understandable to the intended audience, respectively.

### 1.2.1. Problem Identification

This process involves understanding the background and context of the problem. The motivation for this research comes from the significance and potential impact of solving the problem. It is a crucial step in the DSRM model as it sets the direction for the entire research project and helps to ensure that the findings are relevant and useful.

The left ventricle segmentation process is a complicated task, because it brings challenges such as the complex anatomy of the heart, variations in image quality, and the need for high precision. To make the complicated anatomy of the heart more understandable, we made a brief explanation of the cardiac cycle and structure.

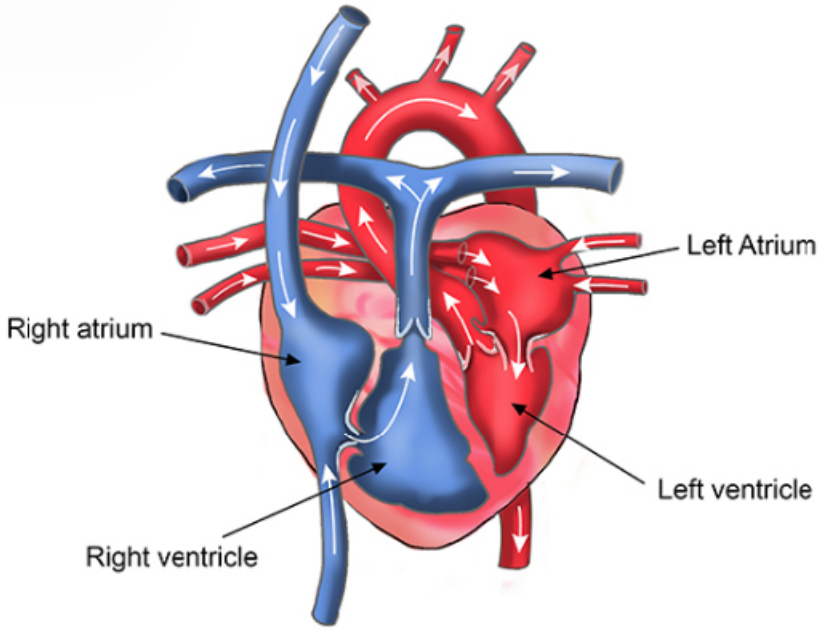



FIGURE 1.2. The Heart's Chambers (taken from [**9**])

The heart has four chambers as we can see in Figure 1.2. The two top chambers that receive blood are known as the atria or atriums. The ventricles are the two bottom chambers of the heart that are responsible for ejecting blood. These chambers work together to provide appropriate blood flow throughout the body. The **right atrium**, which is positioned in the upper right section of the heart, receives blood from the body, entering through two veins: the superior vena cava in the upper body and the inferior vena cava in the lower body. Blood travels from the right atrium to the right ventricle via a valve. The **right ventricle**, located in the lower right chamber of the heart, is the second chamber where blood enters and it pumps blood to the lungs. The lungs oxygenate blood before returning it to the heart through the left atrium. The **left atrium** is located in the top left quadrant and it accepts oxygenated blood from the lungs. When blood enters the left atrium, it travels via a valve into the left ventricle. The **left ventricle**, located in the lower left portion of the heart, pumps oxygenated blood into the body. It

is the final chamber where blood enters. When blood enters the left ventricle, it is driven through the aortic valve and into the aorta, distributing blood throughout the body. The left ventricle is the most strong and muscular chamber, and it is responsible for pumping blood throughout the body [**9**].

When it comes to the layers of the heart, the heart wall is composed of three layers: epicardium, myocardium and endocardium. The **epicardium** is a thin, smooth protective layer that covers the outer surface of the heart; The **myocardium**, also known as MYO, is the middle layer of the heart wall. It is principally responsible for the heart's contraction and makes up roughly 95% of the heart's thickness; The **endocardium** is the deepest layer of the heart wall. It lines the heart chambers and protects the valves.

These cardiac structures perform critical functions in regulating the blood pumping throughout the body during each cardiac cycle which contains two phases: diastole and systole. During **diastole**, which begins with the closure of the aortic valve and ends with the closing of the mitral valve, both ventricles are relaxed and can fill with blood. The conclusion of diastole marks the heart's maximal volume. **Systole**, on the other hand, refers to the phase of the cardiac cycle marked by ventricular contraction and the ejection of blood via the valves, where the mitral valve is closed first, and then the aortic valve is opened. The end of systole indicates the conclusion of the contraction phase and the heart's minimal volume.

Because our purpose is to focus on the left ventricle, we could go into further depth about it and outline its three major regions: basal, mid, and apical regions.

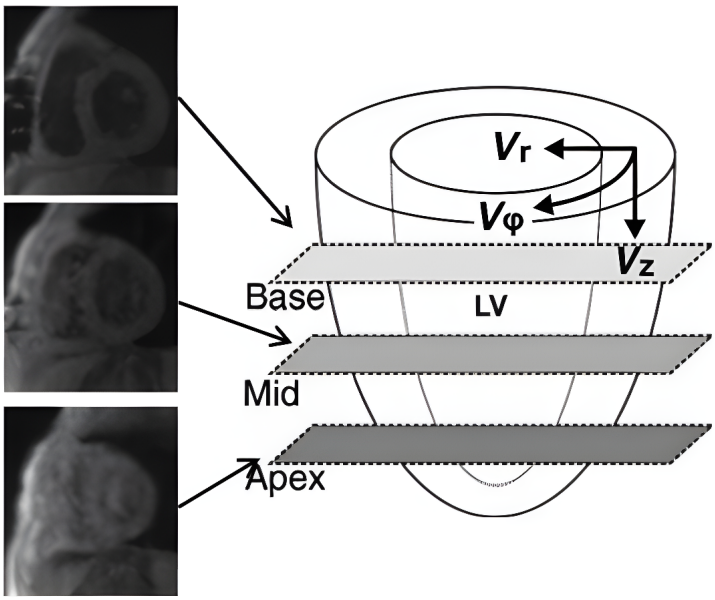



FIGURE 1.3. Acquisition of basal, mid, and apical slices (taken from [**10**])

The **basal slice** is the area of the heart closest to the bottom or top of the left ventricle, usually around the link to the atria; The **mid slice**, also known as the mid-cavity slice,

is a part of the left ventricle located between the apex and base of the heart, about in the center of the ventricle; The **apical slice** represents the apex or tip of the left ventricle.

While short-axis view is critical for assessing wall thickness, chamber size, and regional function, the long-axis view provides a full view of the LV from apical to base, showing overall form, size, and longitudinal structural anomalies.

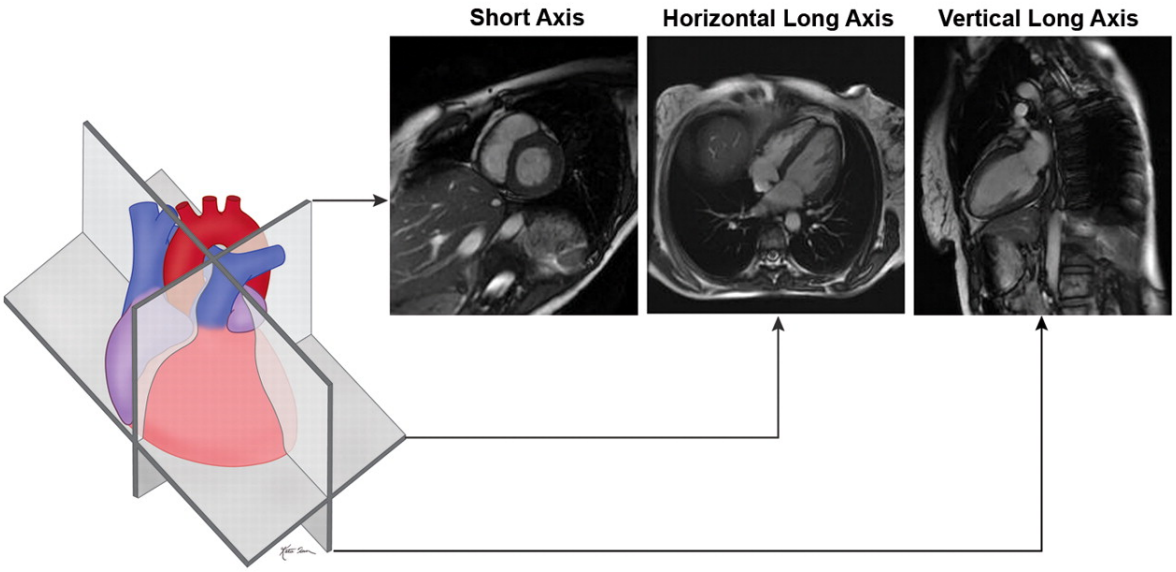



FIGURE 1.4. MRI in three different cardiac planes (taken from [**11**])

A MRI can be obtained from three different cardiac planes such as the short axis, horizontal long axis (four-chamber view), and vertical long axis (two-chamber view) as we can see in Figure 1.4. These planes are determined using axial body plane pictures, running from the cardiac apex to the mitral valve center [**11**]. At the mid level of the left ventricle, the short-axis plane is perpendicular to the real long-axis. The horizontal long-axis is perpendicular to the short-axis, while the vertical long-axis is orthogonal to the short-axis plane [**12**]. The vertical long-axis view is especially useful for examining the left atrial and left ventricle chambers, and the inferior walls of the left ventricle. In contrast, the horizontal long-axis view is useful for assessing all four chambers of the heart, the septal and lateral walls of the left ventricle [**13**]. Throughout this project, we used the vertical long-axis view to give us a better view for comprehensive evaluation of the left ventricle and longitudinal cardiac function.

We believe that combining short-axis and long-axis techniques can improve the accuracy of left ventricle segmentation through the combination of precise cross-sectional anatomical and functional data from the short axis with complete structural and longitudinal information from the long axis. This combination of factors offers more exact border delineation, improved volumetric measures, and better identification of both regional and global cardiac anomalies.

### 1.2.2. Research Questions

There are several research questions that can be addressed in this research, but the most important are:

1) Are current algorithms for left ventricle segmentation the most effective?

2) How can active contour models improve left ventricle segmentation?

3) Can we accurately recreate the left ventricle in the long-axis orientation using segmentation data acquired from the short-axis images?

These questions help to define the scope and direction of the research and help clarify the objectives of this dissertation defined previously.

### 1.2.3. Design and Development

This phase of research requires multiple processes, such as data collection where we collect the necessary data for the problem; data preparation where we clean, pre-process, and transform the data to make it usable for analysis; model creation that involves model selection, model training, model validation, and model fine-tuning where a model is selected and then will be trained, evaluated and adjusted to obtain the best possible performance.

In order to summarize the work to be developed, we can use the pipeline illustrated in Figure 1.5. In a first phase, a process of segmentation of the left ventricle is carried out through a U-Net convolutional neural network [**25**]. This neural network is pre-trained with the information extracted from the datasets used along the pipeline. After that, an Active Contours model is applied with the purpose of enhance boundaries to a smoother shape, reduce granularity, and maintain accuracy. All these processes are carried out with short-axis images and, in the end, we retrieve the main segmentation accuracy metrics so we can compare the performance of different pipeline steps.

As we intend also to do the segmentation process in long-axis, we proceed to a radial long-axis reconstruction that allow us to perform a conversion from short-axis to long-axis. After performing this process, we use the resulting coordinates and we use our active contours model to refine the segmentation, allowing the snakes to dynamically adjust to the real anatomical shape of the left ventricle.

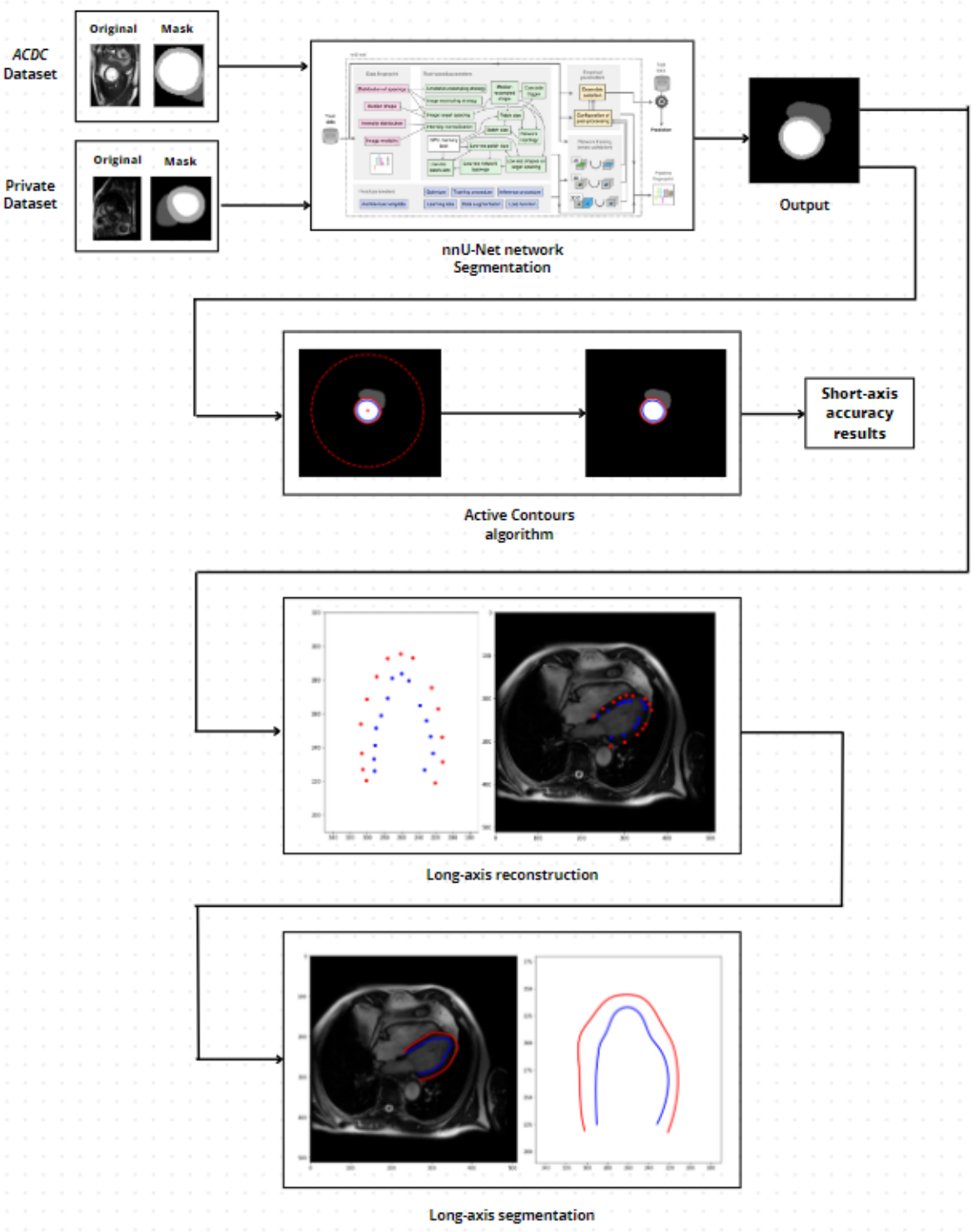



FIGURE 1.5. Proposed Pipeline

### 1.2.4. Thesis organization

This thesis is divided into five chapters, each with a specific objective. The Chapter 1. Introduction establishes the context and reason for the thesis while also clarifying the research issues and methods. The Chapter 2. Literature Review provides a complete review of cutting-edge techniques for segmenting left ventricle (LV), as well as the long-axis

reconstruction and segmentation procedure. The Chapter 3. Methodology presents the dataset used, followed by an explanation of the architecture used to perform short-axis segmentation. The proposed method to perform long-axis reconstruction and segmentation is also presented. The Chapter 4. Results and Discussion focuses on presenting the results and respective discussion about the methods introduced before. Finally, the Chapter 5. Conclusions includes closing remarks, responses to research questions, and recommendations for further study and improvements.

### 1.2.5. Contributions

This thesis proposes some contributions to the field of cardiac image segmentation. In the scope of work, multiple artefacts were proposed and implemented and as a result we were able to make contributions such as a highest approximation of the real left ventricle shape and achieve a high level of accuracy for the short-axis segmentation model. In addition, we were able to contribute with an original method of left ventricle reconstruction and segmentation in long-axis.

All of these contributions were create using our suggested pipeline, which may segment and provide important information for LV function evaluation.

CHAPTER 2

# Literature Review

In this chapter, we review related work that provides a comprehensive overview of the existing knowledge on the subject of this study. The purpose of this chapter is to gain a better understanding of the intended topic and build a strong foundation for the research being conducted.

In a first phase, we searched multiple databases and sources for relevant studies, and we concluded that the most efficient and easy to use are Google Scholar and IEEE. We started by performing a general search using the keywords "Automated Cardiac Segmentation", without applying any filtering criteria. At this phase, we collected 89 articles directly or indirectly related to the keywords used in research. This number is high, so we must ensure that we select only the articles that go exactly according to the desired criteria.

In the second phase, to ensure a higher quality of information, the following inclusion criteria were applied:

- Articles published in English.
- Articles exclusively related to the left ventricle.
- Articles focused on the use of MRI.

These filtering criteria help to improve the accuracy and credibility of the research results. All articles must be in English, so that it is easy to read. Before 2016, there were no articles that had considered deep learning methods related to cardiac segmentation, so all articles prior to this year were ignored. Finally, we had to adapt the collected articles to the objectives of this dissertation and, therefore, all articles that are not related to the left ventricle or the use of MRI images were excluded.

The results of applying the filtering criteria can be illustrated in Table 2.1.

Table 2.1. Number of articles collected per research phase

| **Literature Review** | **Number of articles collected** |
|---|---|
| Without filtering criteria | 89 |
| With filtering criteria | 51 |

Table 2.1 shows the number of articles collected depending on filtering criteria. The articles collected by applying the filtering criteria are those used in this project.

## 2.1. Segmentation

Accurate segmentation of the cardiac structures is a crucial part of the process and may supply relevant advancements in predicting and controlling different cardiovascular diseases.

### 2.1.1. Classical Segmentation Methods

One of the most used methods in the left ventricle segmentation is the Region of Interest (ROI) detection. The LV has some distinct features within the MRI Image that are exploited in order to identify the ROI, as the heart cavity containing the LV is near the center of the MRI Image, there is a degree of pixel variance around the LV muscle, and the LV is circular in shape. All images are cropped automatically to the region whose center is the centroid of the LV cavity and their size will vary according to the patient. The first research uses 176 x 176 images with the assumption that the LV would be within that area [**17**]. There are also other researches that use different sizes, such as 96 x 96 images [**14**], 25 x 25 images [**17**] or 128 x 128 images [**16**].

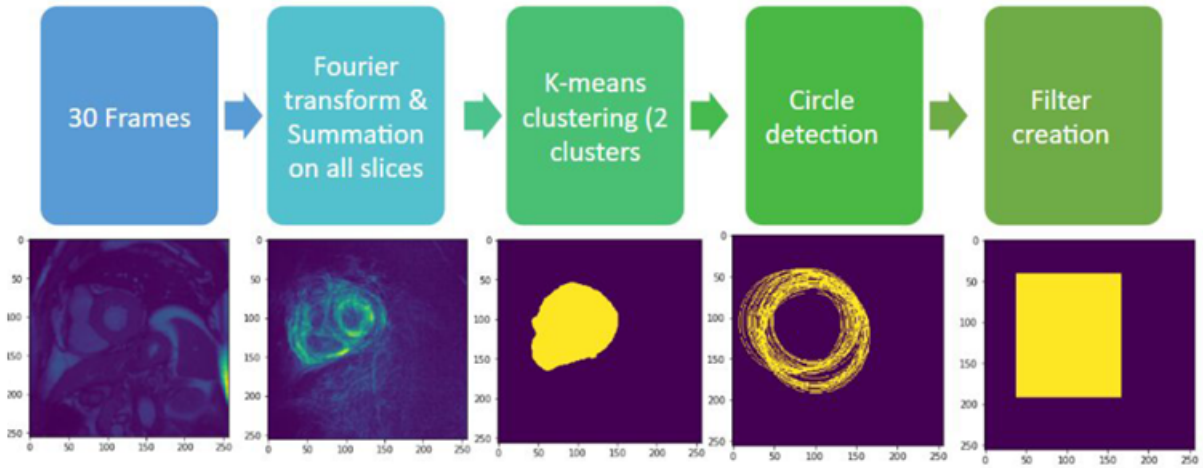



FIGURE 2.1. Steps of Region of Interest (ROI) detection (taken from [**17**])

The Region of Interest detection can be done in several ways and Figure 2.1 shows one of that examples. Fourier Time Transform was applied to pre-processed images and then all the first harmonics for each slice of MRI image were added together across all slices. Next, k-means clustering was performed on the image resulting from summing the first harmonic of all slices where high values indicate where the left ventricle was present. As we know the LV has a circular shape, so a circle detection was made and finally a filter was created indicating the final region of interest [**17**].

### 2.1.2. Evaluation Metrics

The evaluation metrics provide a comprehensive evaluation of the segmentation accuracy and are typically used to compare different LV segmentation algorithms and to assess the performance of an algorithm on a specific dataset. There are many metrics that can be used in the segmentation method [**17**].

The metrics focused on the mathematical and spatial accuracy of the segmentation itself are:

- Dice Similarity Coefficient (DSC):

$$DSC = 2(Ytrue \cap Ypred)/(|Ytrue + Ypred|) \tag{2.1}$$

This metric (DSC) computes the spatial overlap between the reference volume manually segmented (Ytrue) and the corresponding automatically segmented volume (Ypred). The result value may vary from 0 (mismatch) to 1 (excellent match) [**17**].

- Jaccard Similarity Coefficient (JSC):

$$JSC = (Ytrue \cap Ypred)/(|Ytrue \cup Ypred|) \tag{2.2}$$

The JSC, also known as Jaccard index, is a measure of the similarity between two sets of data. In this case, the similarity between the real set of data (Ytrue) and the automated set of data (Ypred) was measured. It ranges from 0 to 1, with a value of 1 indicating that the sets are identical, and a value of 0 indicating that they have no elements in common [**17**].

- Hausdorff Distance (HD):

$$HD = \max_{a_i \in A} \min_{m_j \in M} ||a_i - m_j|| \tag{2.3}$$

The HD computes the degree of mismatch between A and M by calculating the Euclidean distance of each point $a_i$ that is most distant from any point $m_j$. A represents the set of points generated by the algorithm used, while M represents the set of manually generated points. Smaller HD means better segmentation. In order to minimize the difference between sampling densities of sets, a linear subdivision operator to the surface containing the lowest number of vertices was applied [**20**]. As opposed to several MRI cardiac segmentation papers which report 2D Hausdorff distances [**21, 22**], the most recent studies report the 3D Hausdorff distances, which allows an intrinsic management of the missing segmentation problem on the end slices by highlighting the worst-case deviations, ensuring a comprehensive and fair evaluation of segmentation performance [**16, 20**].

- Absolute Volume Difference (AVD):

$$AVD = |Vpred - Vtrue| \tag{2.4}$$

The Absolute Volume Difference calculates the difference between the left ventricle volume generated by the algorithm (Vpred) and the manual LV volume (Vtrue) [**16**].

- Average Perpendicular Distance (APD):
The Average Perpendicular Distance measures the distance from the automatically segmented contour to the corresponding manually drawn expert contour, averaged over all contour points [**21**].

These metrics will depend on the stage in which the heart is. The cardiac cycle is composed by 2 phases, systole, and diastole. The diastolic phase (ED) ends at a specific moment in the heart cycle, signaling the termination of the relaxation phase. In the same manner, the end of the systolic phase (ES) indicates the end of the contraction phase.

We can implement three indices for the clinical parameters, namely the correlation (corr), the bias and the standard deviation (std) values. These metrics are computed from the measurements of:

- End-diastolic volume (EDV, expressed in mL/$m^2$). This metric refers to the amount of blood present in the ventricles of the heart at the end of diastole. Abnormalities in EDV can indicate various heart conditions, such as heart failure or valvular diseases.
- End-systolic volume (ESV) is the amount of blood remaining in the ventricles of the heart at the end of systole. A high ESV can indicate that the heart is not functioning optimally, which can be a sign of heart disease, heart failure, or other cardiac conditions.
- Ejection fractions ($LV_{EF}$ expressed in percent for the LV). It is the measure of the amount of blood pumped out of the ventricles of the heart with each heartbeat. A normal EF is around 55-70%. It can be calculated by the following formula:

$$EF = (EDV - ESV)/EDV \tag{2.5}$$

- Myocardium mass (MYMass expressed in g/$m^2$ and calculated in diastole). Myocardium mass refers to the total weight or mass of the heart muscle, also known as the myocardium. The myocardium is the thick, muscular layer of the heart that is responsible for contracting and relaxing to pump blood through the body. An increase in myocardium mass can indicate heart disease, such as hypertensive heart disease or cardiomyopathy, while a decrease in myocardium mass can indicate heart failure or other conditions that affect the heart's ability to pump effectively.

These metrics are quantitative measurements derived from the LV segmentation results, which provide information about the size, shape, and function of the LV.

### 2.1.3. Deep Learning Segmentation Architectures

Deep learning techniques have gained popularity in LV segmentation lately, due to their capability of efficiently processing and dissecting massive amounts of image information. Since we knew from prior information that deep learning methods are the most successful in this kind of problem and as it was included in the search filtering criteria, only research articles including deep learning architectures for the automatic segmentation of the left ventricle were considered.

There are several existing deep learning methods for LV segmentation, including Convolutional Neural Networks (CNNs) [**23**], Recurrent Neural Networks (RNNs) [**27**], and Generative Adversarial Networks (GANs) [**28**]. CNNs, which are widely used in medical image analysis, can effectively identify and extract features from the LV images. RNNs, which are used to analyze sequential data, have also been applied to LV segmentation to handle the temporal information in cardiovascular images. GANs, which involve the

training of two neural networks, have been used for data augmentation and to improve the performance of LV segmentation models.

These deep learning approaches have exhibited encouraging outcomes in LV segmentation, displaying high precision and consistency across diverse datasets.

**Convolutional Neural Networks**

Convolutional Neural Networks (CNNs) are a type of deep learning method that have been widely used in medical image analysis, including left ventricle (LV) segmentation, and are composed of multiple layers, each executing a designated task [**23**]. The achievements of Convolutional Neural Networks (CNNs) in LV segmentation are due to their aptitude for comprehending intricate image characteristics and automatically drawing relevant information from medical imaging [**7, 22, 24**].

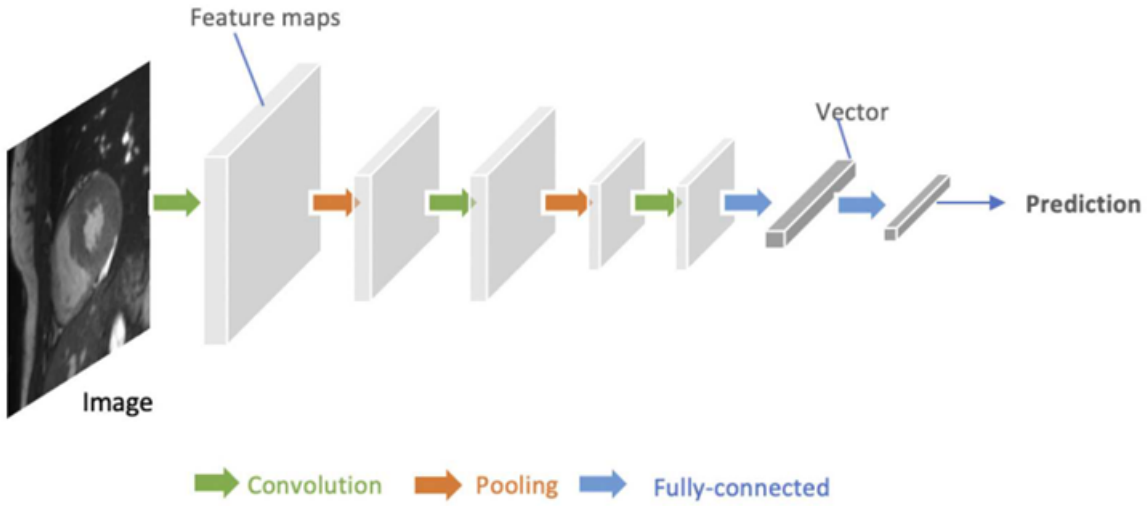



FIGURE 2.2. Generic architecture of convolutional neural network (taken from [**24**])

As show in Figure 2.2, a standard CNN consists of an input layer, an output layer, and a stack of functional layers. These functional layers often contain convolutional layers, pooling layers and/or fully connected layers. Typically, a convolutional layer contains multiple convolution kernels/filters, preceded by a normalization layer and a non-linear activation function for producing multiple feature maps from the input. The feature maps are subsequently reduced in size through pooling layers, often by a factor of 2, which eliminate redundant information to enhance the statistical efficiency and model generalization. Subsequently, fully connected layers are utilized to lower the dimension of features from the preceding layer and identify the most pertinent features for the task at hand. The final result of the network is a fixed-sized vector, where each component can represent a set of values (e.g., the bounds of a bounding box for left ventricle detection and localization in segmentation process) [**24**].

There are several CNN architectures that have been applied to LV segmentation, like SegNet [**24**] or U-Net [**25**]. These networks differ in their architectures and training

strategies, but they all aim to learn the complex relationships between image pixels and the LV region.

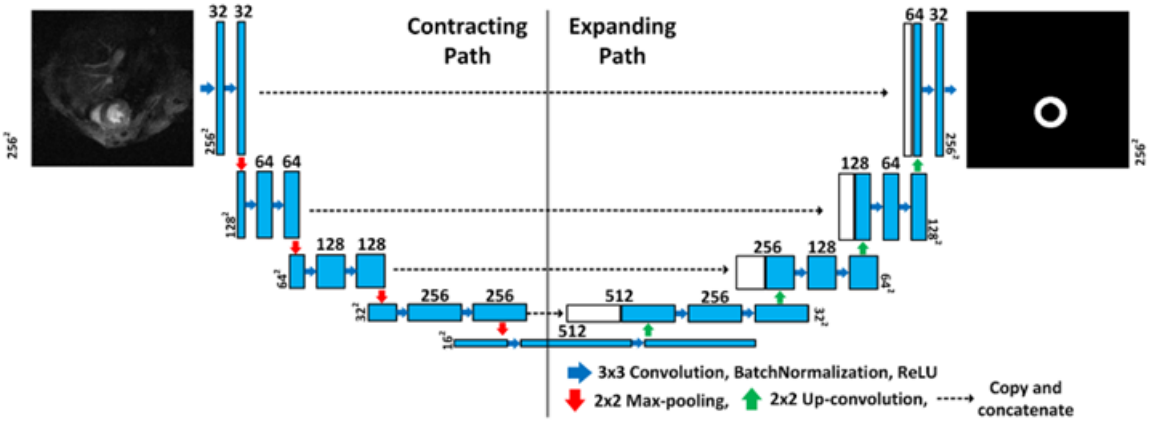



FIGURE 2.3. U-Net architecture for LV segmentation (taken from [**25**])

Figure 2.3 shows an example of an U-Net architecture that is a popular deep learning architecture for image segmentation tasks, including left ventricle segmentation. The U-Net architecture has a symmetrical design, with the encoding and decoding parts connected by skip connections. The skip connections allow the network to maintain the fine details of the input image while also using the higher-level information captured in the lower dimensional representation. In the encoding stage, a series of convolution and downsampling layers are employed to compact the input image while retaining critical information. The decoding phase uses transposed convolutions to increase the resolution back to the original image dimensions. The output from the encoding stage is combined with the decoder through skip connections to recover high-resolution details. Further refinements to the prediction are made with extra convolutional layers in the decoder. The network produces a pixel-wise classification map, where each pixel is categorized as either part of the left ventricle or not.

Fully Convolutional Neural Networks (FCNNs) are a popular type of CNN utilized for image segmentation purposes, including left ventricle segmentation. FCNNs are crafted to work on images and generate pixel-level predictions without the usage of fully connected layers, thereby allowing them to process images of any dimension and retain high-resolution predictions. The application of FCNNs in LV segmentation has produced encouraging results in several research studies [**14, 15, 17, 26**], demonstrating high precision and consistency.

### Recurrent Neural Networks

Recurrent Neural Networks (RNNs) are a type of artificial neural network that have been widely used in various applications, including natural language processing, speech recognition, and time-series prediction. In medical image analysis, RNNs have shown promising results in left ventricle segmentation [**27**]. RNNs are ideal for this left ventricle segmentation task as they can effectively learn and utilize temporal relationships and

historical information. This enables the RNNs to identify the spatial and temporal characteristics of the left ventricle, ultimately leading to a segmentation map that precisely distinguishes it from neighboring tissues [**26, 27**].

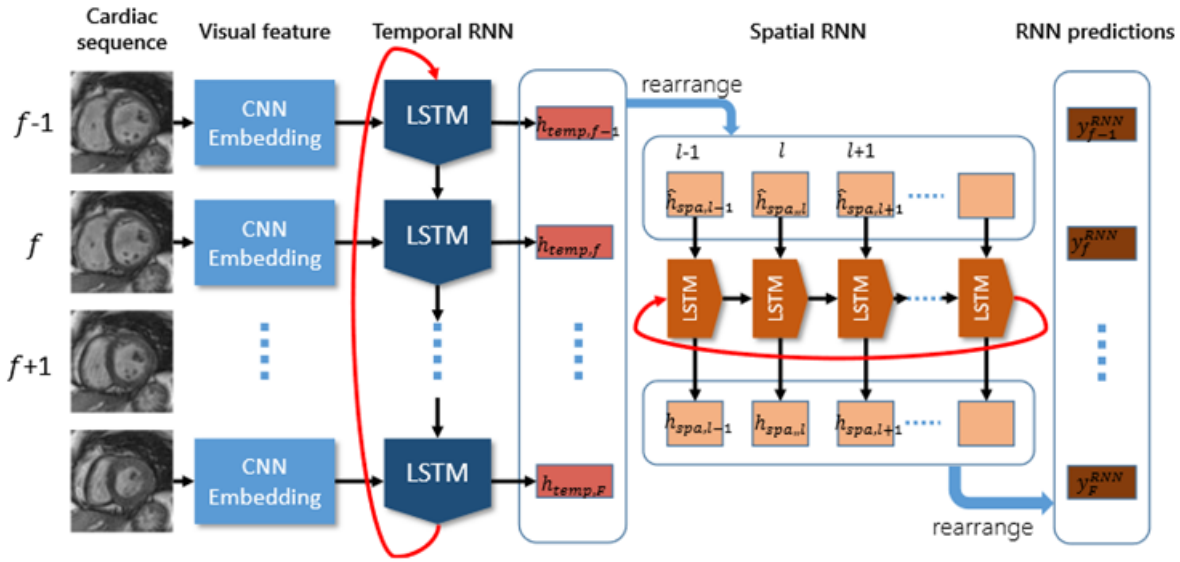



FIGURE 2.4. RNN Architecture for LV Segmentation (taken from [**27**])

The inter-frame relationships are modeled through the use of a temporal-RNN that takes CNN-generated features as input. The spatial relationships among neighboring regions are then modeled using a spatial-RNN, which takes the output of the temporal-RNN as input and rearranges it.

### Generative Adversarial Networks

Generative Adversarial Networks (GANs) are a class of deep learning models that consist of two components: a generator and a discriminator. In left ventricle segmentation, GANs can be used to generate realistic synthetic images that can be used to train and evaluate the performance of the segmentation models [**28**].

The implementation of GANs in left ventricle segmentation helps to address the limitations associated with relying solely on real images for training. The synthetic images generated by the GAN can serve as supplementary training data, help to balance the dataset, and mitigate the effects of limited data. Furthermore, the use of GANs allows for expanding the dataset and investigating various representations of the left ventricle, leading to more dependable and adaptable segmentation models [**28, 29**].

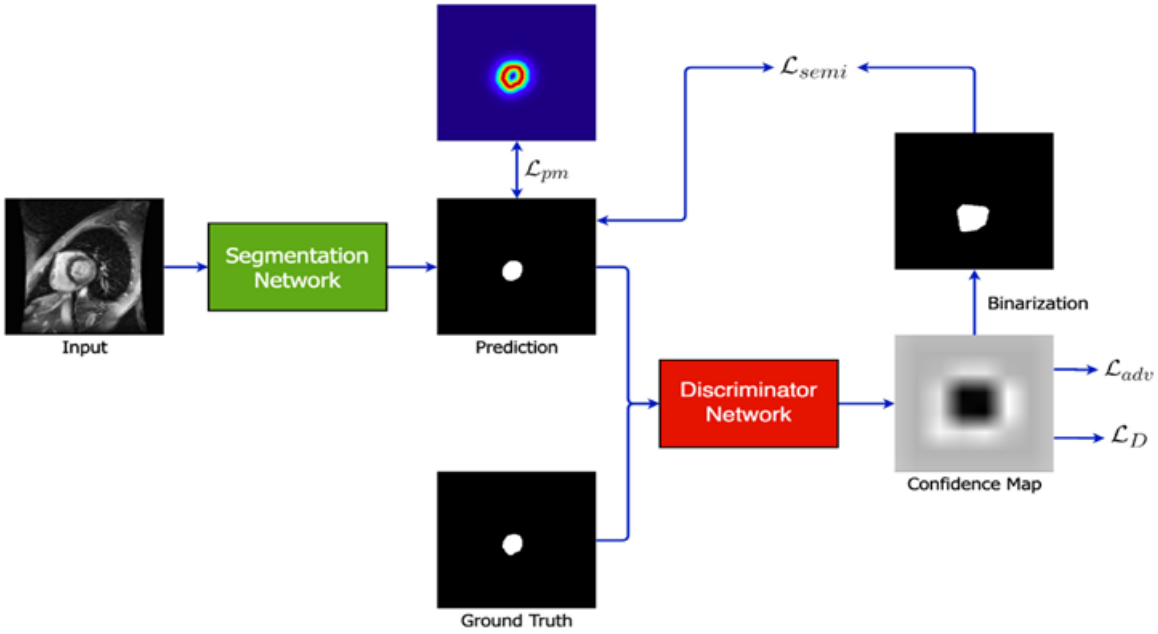



FIGURE 2.5. GAN architecture for LV segmentation (taken from [**28**])

We can identify the generator and discriminator in Figure 2.5. The generator component creates synthetic images, while the discriminator component evaluates the realism of these images and provides feedback to the generator. The aim of the generator is to generate images that closely resemble actual images, while the discriminator strives to differentiate between real and synthetic images with precision. During the training process, the generator and discriminator engage in a continuous competition, with the generator constantly striving to produce increasingly lifelike images, and the discriminator working to improve its accuracy in separating real images from synthetic ones.

### 2.1.4. Segmentation Results Analysis

In order to compare the efficiency between the main deep learning architectures, a table was created that shows the different results for the main articles related to left ventricle segmentation. All of these methods used the Automated Cardiac Diagnosis Challenge (ACDC) dataset [**20**].

The results reported in Table 2.2 were important to compare the left ventricle segmentation accuracy with our proposed method that also used ACDC dataset. This dataset is a publicly available dataset used for evaluating the performance of algorithms for the automated analysis of cardiac MR images. The dataset contains a large number of cardiac MR images acquired from patients with various cardiovascular conditions, such as dilated cardiomyopathy, myocardial infarction, and healthy controls.

TABLE 2.2. Segmentation accuracy of the main articles studied and verified on the ACDC dataset

| Method | Description | ED LV | | ES LV | |
|---|---|---|---|---|---|
| | | DSC | HD | DSC | HD |
| Isensee et al.[**30**] | 2D U-net + 3D U-net | 0.968 | 7.4 | 0.931 | 6.9 |
| Baumgartner et al.[**31**] | 2D U-net with cross entropy loss | 0.963 | 6.5 | 0.911 | 9.2 |
| Jang et al.[**32**] | 2D M-Net with weighted cross entropy loss | 0.959 | 7.7 | 0.921 | 7.1 |
| Zotti et al.[**33**] | 2D GridNet with registered shape prior | 0.957 | 6.6 | 0.905 | 8.7 |
| Khened et al.[**34**] | 2D Dense U-net with inception module | 0.964 | 8.1 | 0.917 | 9.0 |
| Rohé et al.[**35**] | Multi-atlas based method combined with 3D CNN | 0.957 | 7.5 | 0.900 | 10.8 |
| Yang et al.[**36**] | 3D FCN with deep supervision | 0.864 | 47.9 | 0.775 | 53.1 |
| Decourt e Duong[**28**] | DT-GAN | 0.870 | 2.53 | 0.890 | 2.6 |

From the results presented in Table 2.2, we can understand that Isensee et al. [**30**] achieved the top performance relatively to Dice Similarity Coefficient values. This means that it is the method that shows a better similarity between test and train sets. Despite having a lower DSC, the method proposed by Decourt e Duong [**28**] presents the best performance in relation to Hausdorff distance, because a smaller HD means better segmentation.

## 2.2. Active Contour Models

Active contour models [**37**] represent methods used for object segmentation in digital images. They are also referred to as snakes or deformable contours. When it comes to tasks like left ventricle segmentation in medical imaging, these models are especially helpful. In this situation, active contour models aid in defining the left ventricle's borders within cardiac imaging, which is crucial for identifying heart problems and assessing the organ's health.

The main objective of active contour models is to automatically and precisely trace the border or contour of an object of interest using a smooth curve. To minimize an energy or cost function that gauges how well the contour lines up with the desired object boundaries, a contour is iteratively deformed in this method. When the item of interest has complicated or irregular features, active contour models are especially useful [**37**].

The left ventricle segmentation process in cardiac imaging is one task where active contour models give a semi-automated strategy that has a great flexibility to complex forms advantage. However, parameter tuning and initialization continue to be obstacles to obtaining reliable and accurate findings. Although there are now alternative methods for segmenting the left ventricle thanks to developments in deep learning and convolutional neural networks, active contour models are still a useful resource in the field of medical image analysis [**37**]. In Figure 2.6, we can find an example of an active contour model.

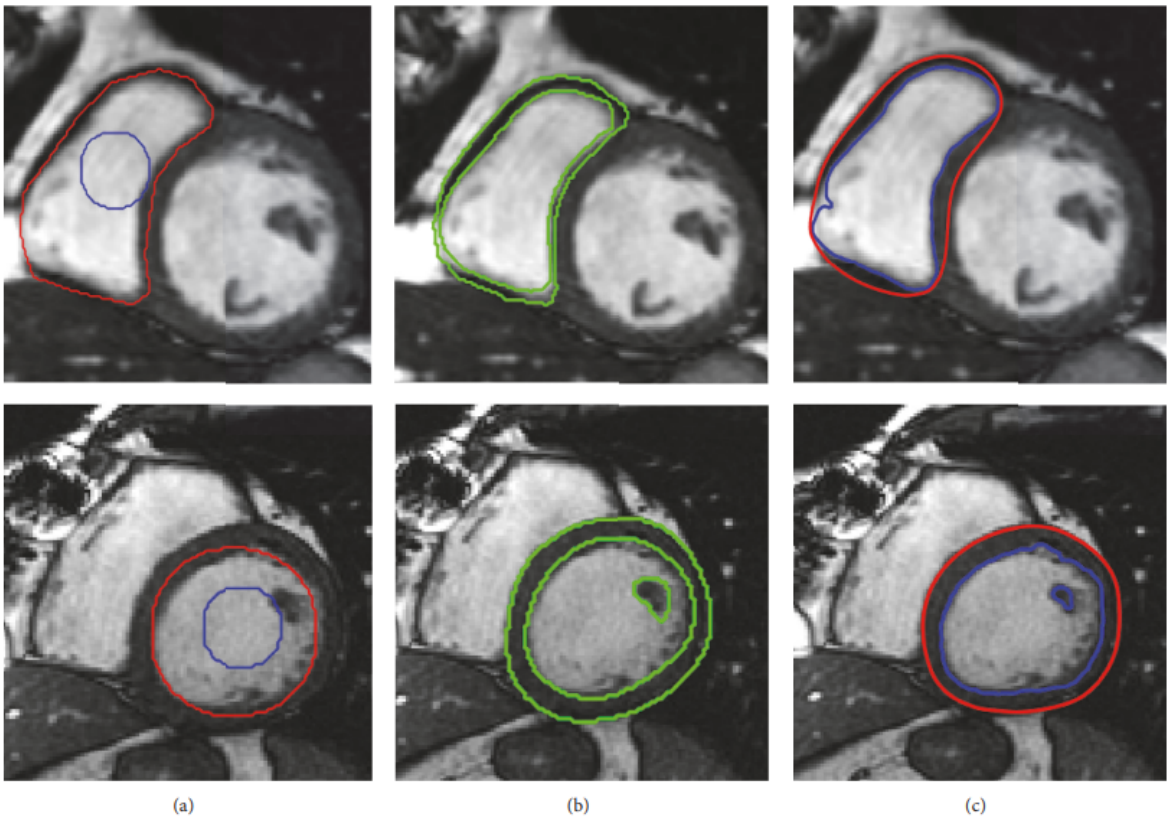



FIGURE 2.6. Active Contour Model example. (a) Initialization contours, (b) ground truth, and (c) final segmentation result (taken from [**38**])

This active contour method uses both local and global image statistical information. In a first phase, an energy functional is devised using a new region-based SPF function based on Lankton and Tannenbaum [**39**] and Min et al.[**40**] intensity terms, which drives the zero level set curve towards the object boundary. During the curve evolution, its movement depends on the sign of the SPF function, which moves inwards if SPF is positive and outwards if it is negative. This leads to the initial contours drawn in Figure 2.6 (a). It is vital to notice that this approach can offer different types of curves rather than only sharp curves.

The left ventricle's borders inside a particular medical image are represented pixel-by-pixel in the ground truth (represented in Figure 2.6 (b)) in the form of a binary image or label map. Each pixel in the image is given a name in this format to show whether it is a part of the background tissues or the foreground left ventricle. Medical professionals or skilled annotators manually segment the left ventricle in the original medical pictures to produce these ground truth images. To precisely delineate the boundaries surrounding the left ventricle, they employ specialist software or sketching tools.

In the last phase, a Gaussian kernel is used, which not only regularizes the level set curve but also removes the computationally expensive reinitialization step. All these steps are an example of an active contour model whose final result of segmentation can be seen in the Figure 2.6 (c) [**38**].

## 2.3. Radial Long-axis Reconstruction and Segmentation

In the field of cardiovascular magnetic resonance imaging, long-axis reconstruction is not particularly extensive-depth since the segmentation process is more complex, because it is not a close curve. However this process is vital for enhancing our understanding of heart architecture and function. While precise cross-sectional views of the heart are provided by short-axis MRI slices, the anatomical and functional details along the longitudinal axis of the heart may not be completely captured so long-axis reconstruction is useful in this situation.

Long-axis reconstruction is the technique of creating pictures that show the structure of the heart along its longitudinal axis by reformatting the segmented contours of the left ventricle from several short-axis slices. Specialized software and algorithms can be used to conduct this reconstruction, interpolating the contours to create continuous long-axis views. In long-axis reconstruction, the left ventricle's segmented information from short-axis MRI scans is converted into a set of long-axis pictures that reveal the structure and motion of the heart in the longitudinal plane. These long-axis images enable researchers and healthcare workers to gain a greater understanding of the activity of the heart during the cardiac cycle.

Although there is no specific radial long-axis reconstruction method for the left ventricle to the best of our knowledge, there are some methods related to the right ventricle [**41**] such as the one illustrated in Figure 2.7.

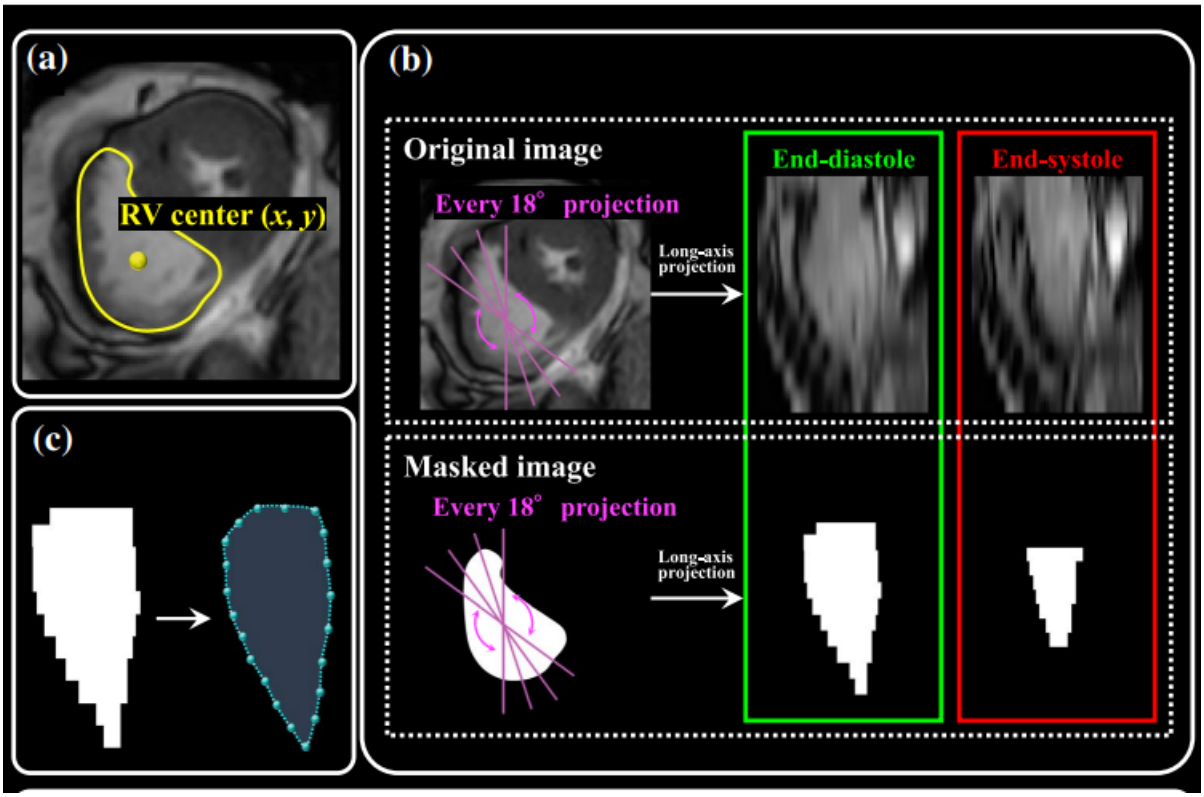



FIGURE 2.7. Radial long-axis reconstruction example (taken from [**41**])

This figure illustrates a radial long-axis reconstruction of short-axis images and their manually segmented right ventricular regions.

In the first step (Figure 2.7 (a)), the RV region's centroid was defined as the $x$ and $y$ coordinates of the RV center in the middle slice of the heart at the end-systolic frame. The middle slice of the heart was selected automatically as the slice between the first basal and last apical slices. In the second step (Figure 2.7 (b)), radially around the RV centroid, long-axis pictures were recreated. Following that, ten long-axis images were reconstructed every 18° using radial projection. By using nearest-neighbor interpolation, the reconstructed long-axis pictures were enlarged to 128x128. These reconstructions were made on short-axis (SA) pictures at the end of diastole and end of systole. The reconstructed RV pictures were converted into binary images using a customized threshold approach, and the coordinates of the binary region's edge were automatically collected. Thereafter, the number of coordinates was automatically replaced with 100 at even intervals. After that, the RV region in the long-axis image was designated by a curve that connected 100 points smoothly using spline interpolation as we can see in Figure 2.7 (c). Because the RV area of the long-axis was smaller than that of the SA, a dilation technique using 3.0 line-shaped structuring elements was used. In this work, the dilation parameter was chosen to have the best RV area agreement with manual measurements. The dilatation processing is thought to be required because the RV regions may have been under-extracted during the picture reduction procedure for deep learning. Finally, at the end of diastole and the end of systole phases, radially reconstructed long-axis pictures show the right ventricular contour as a spline interpolated line [**41**].

Although this example is intended for the right ventricle, the process of radial long-axis reconstruction of the left ventricle is very similar. Long-axis images, in particular, provide a comprehensive view of the LV, allowing for an accurate estimate of its size and shape. To ensure that these segmentation algorithms are clinically useful, it is essential to employ rigorous evaluation metrics that quantify the accuracy, robustness, and clinical relevance of LV segmentation in long-axis cardiac images.

In addition to the evaluation metrics related to the short-axis images, we can also define two other metrics: Global Longitudinal Strain [**42**] and Long-Axis Strain [**43**]. These metrics are connected to cardiac segmentation, although they are not segmentation assessment metrics themselves. Instead, these measures are linked to a functional study of the left ventricle based on cardiac muscle longitudinal deformations.

- Global Longitudinal Strain (GLS):

$$GLS = ((L - L0)/L) \times 100\% \tag{2.6}$$

  GLS is a robust, well validated and reproducible technique for the measurement of LV longitudinal deformation [**42**]. Longitudinal deformation refers to the contraction or expansion of the cardiac muscle along the longitudinal axis (i.e., from top to bottom) of the left ventricle during a cardiac cycle. To get its value,

we have to obtain measurements of myocardial length at both end-diastole and end-systole. L represents the initial length of the myocardium (at end-diastole) and L0 represents the final length of the myocardium (at end-systole), both often measured in millimeters.

- Long-Axis Strain (LAS):

$$LAS = ((L2 - L1)/L1) \times 100\% \tag{2.7}$$

LAS is an important metric in cardiac imaging and analysis that examines how the heart muscle elongates and contracts along its long axis [**43**]. To get its value, we have to obtain measurements of myocardial length at both end-diastole and end-systole. L1 represents the initial length of the myocardium at the beginning of the cardiac cycle (usually during end-diastole) and L2 represents the length of the myocardium at a later point in the cardiac cycle (usually during end-systole).

GLS and LAS are both useful tools for cardiac professionals and researchers. They contribute to a full assessment of heart health by enabling for the early diagnosis of cardiac dysfunction, following disease development, and evaluating therapy success.

CHAPTER 3

# Methodology

## 3.1. Datasets

We used two datasets to perform our methodological processes: one publicly available dataset and one privately generated dataset.

The public dataset supplied a well-established baseline, while the private dataset is more realistic since it includes images of actual, known patients, and it is frequently used for diagnosing medical issues everyday. It is important to mention that all data from the private dataset is anonymised to ensure privacy and confidentiality.

### 3.1.1. ACDC Dataset

In the first phase of this thesis, we used the Automated Cardiac Diagnosis Challenge (ACDC) dataset [**20**]. This dataset is public and it was built using genuine clinical tests obtained at the University Hospital of Dijon. The acquired data were properly anonymised and managed in accordance with the guidelines established by the local ethics committee of the Hospital of Dijon (France). This dataset contains enough examples to appropriately train machine learning algorithms and clearly analyze fluctuations in the key physiological parameters collected from cine-MRI (namely diastolic volume and ejection fraction). The dataset consists of 150 examinations (all from separate individuals) sorted into 5 evenly distributed subgroups (4 diseased and 1 healthy). This dataset is divided into two folders: "training" (with 100 examinations that are used to perform the training of the implemented model) and "testing" (with 50 examinations that are used to perform model testing). Each patient also contains the following extra information: weight, height, and diastolic and systolic phase instants.

In this dataset, we have:

- 30 healthy individuals;
- 30 individuals having a prior myocardial infarction (left ventricular ejection fraction less than 40% and multiple myocardial regions with aberrant contraction);
- 30 individuals with dilated cardiomyopathy (diastolic left ventricular volume greater than 100 $mL/m^2$ and a left ventricular ejection fraction less than 40%);
- 30 individuals with hypertrophic cardiomyopathy (left ventricular cardiac mass more than 110 $g/m^2$, numerous myocardial segments thicker than 15 mm in diastole, and normal ejection fraction);
- 30 individuals with an anomalous right ventricle (right ventricular cavity volume greater than 110 $mL/m^2$ or ejection fraction less than 40%).

Each group was precisely classified based on physiological parameters such as left or right diastolic volume or ejection fraction, left ventricle (LV) local contraction, LV mass, and maximal myocardium thickness.

The acquisitions were obtained over a 6 year period using two MRI scanners of different magnetic strengths (1.5 T (Siemens Area, Siemens Medical Solutions, Germany) and 3.0 T (Siemens Trio Tim, Siemens Medical Solutions, Germany)). Cine MR images were acquired in breath hold with a retrospective or prospective gating and with a Steady-State Free Precession (SSFP) sequence in short axis orientation. Particularly, a series of short axis slices cover the LV from the base to the apex, with a thickness of 5 mm (or sometimes 8 mm) and sometimes an interslice gap of 5 mm (then one image every 5 or 10 mm, according to the examination). The spatial resolution goes from 1.37 to 1.68 mm2/pixel and 28 to 40 images cover completely or partially the cardiac cycle (in the second case, with prospective gating, only 5 to 10 % of the end of the cardiac cycle was omitted), all depending on the patient [**18**]. The MRIs, presented in this dataset, have a complete view of the heart and an example of that can be seen in Figure 3.1.

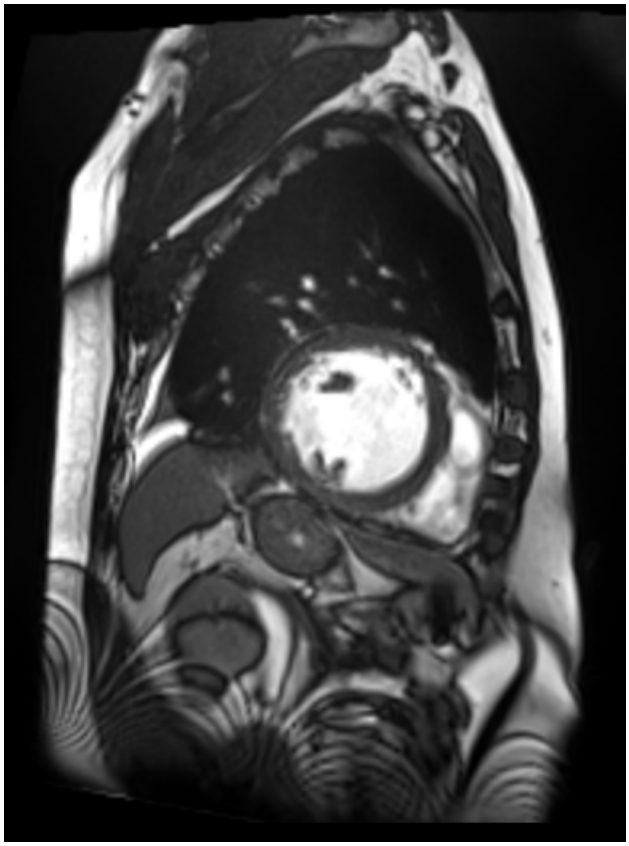


FIGURE 3.1. ACDC dataset image example

The goal of this dataset is, in both end diastolic and end systolic phase examples, compare the performance of automated approaches on the segmentation of the left ventricular endocardium and epicardium as well as the right ventricular endocardium. We chose this dataset, not only because it has the necessary medical images for our research,

but also because it is used in the main articles that serve as standards for evaluating our results.

The ACDC dataset is provided in NIFTI image format [**44**]. This format is derived from an imaging software called ANALYZE [**45**], and both were designed with the goal of storing organized multi-dimensional biological data in a single file. While ANALYZE used separate binary files for header and image data, NIFTI improves upon this by allowing both the header and the 3 or 4-dimensional data to be stored in the same file. With the benefit of combining 3 or 4-dimensional data into a single file, NIFTI is more straightforward and efficient in terms of loading and processing performance than its predecessor ANALYZE.

### 3.1.2. Private Dataset

In the last phase of this thesis, we used a private dataset extracted from one of Affidea's centers in Caselas. This dataset was retrieved and pseudo-anonymized as per Affidea's ethics committee rules. It consists of 30 patients divided equally into two separate diseased categories and a healthy group. Patients were evaluated and classified by professionals in their specialty.

The 30 patients were retrieved from the MRI center's database in Digital Imaging and Communications in Medicine (DICOM) format and evenly distributed across three groups, each with ten patients: NOR (healthy/normal subjects), DCM (dilated cardiomyopathy), and HCM (hypertrophic cardiomyopathy).

This dataset does not give ground truth data for segmentation, but it will serve as a validation, demonstrating the tool's efficacy in diagnosing medical disorders.

## 3.2. Short-axis Segmentation

There are multiple segmentation architectures, as seen in the previous chapter, and therefore it was necessary to find the neural network that presented the best results for any dataset used (in this case, the U-Net network). For that, we used a pre-trained U-Net network called nnU-Net [**46**]. However, the segmentation results can be improved if we add to this network, an active contours model.

### 3.2.1. nnU-Net network

No-new-Net (nnU-Net) is a semantic segmentation method that automatically adapts to a given dataset. It will analyze the provided training cases and automatically configure a matching U-Net-based segmentation pipeline. This network has multiple advantages as: it offers a fantastic out-of-the-box applicable baseline algorithm to compete against; it can act as a method development framework to test our contribution on a large number of datasets without having to tune individual pipelines and it provides a new perspective on the design of segmentation methods. nnU-Net excels in segmentation issues that need training from scratch, such as research applications with non-standard picture modalities and input channels, biological challenge datasets, the bulk of 3D segmentation tasks, and so on.

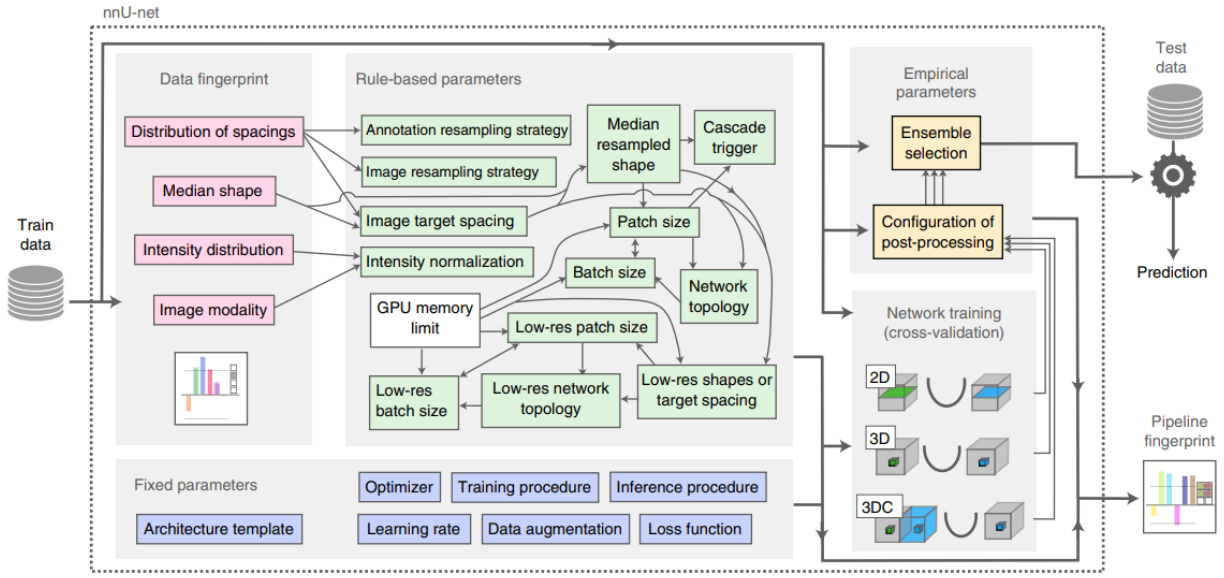



FIGURE 3.2. nnU-Net processes architecture (taken from [**46**])

Not all U-Net configurations are created for all datasets. In datasets with small image sizes, the U-Net cascade is omitted because the patch size of the full resolution U-Net already covers a large part of the input images. This network configures its segmentation pipelines in three main steps as we can see in Figure 3.2:

- Setting fixed parameters that cannot be changed, because during development of nnU-Net, the creators identified a robust configuration (that is, certain architecture and training properties) that can simply be used all the time. This includes, for example, nnU-Net's loss function and learning rate;
- Define rule-based parameters that when using hard-coded heuristic methods, are adjusting key segmentation pipeline features using the dataset fingerprint. For example, the network topology are tailored to the patch size; the patch size, network topology, and batch size are all optimized in tandem given some GPU memory restriction;
- Setting empirical parameters that are essentially trial-and-error. For example the selection of the best U-net configuration for the given dataset (2D, 3D full resolution, 3D low resolution or 3D cascade) and the optimization of the post-processing strategy.

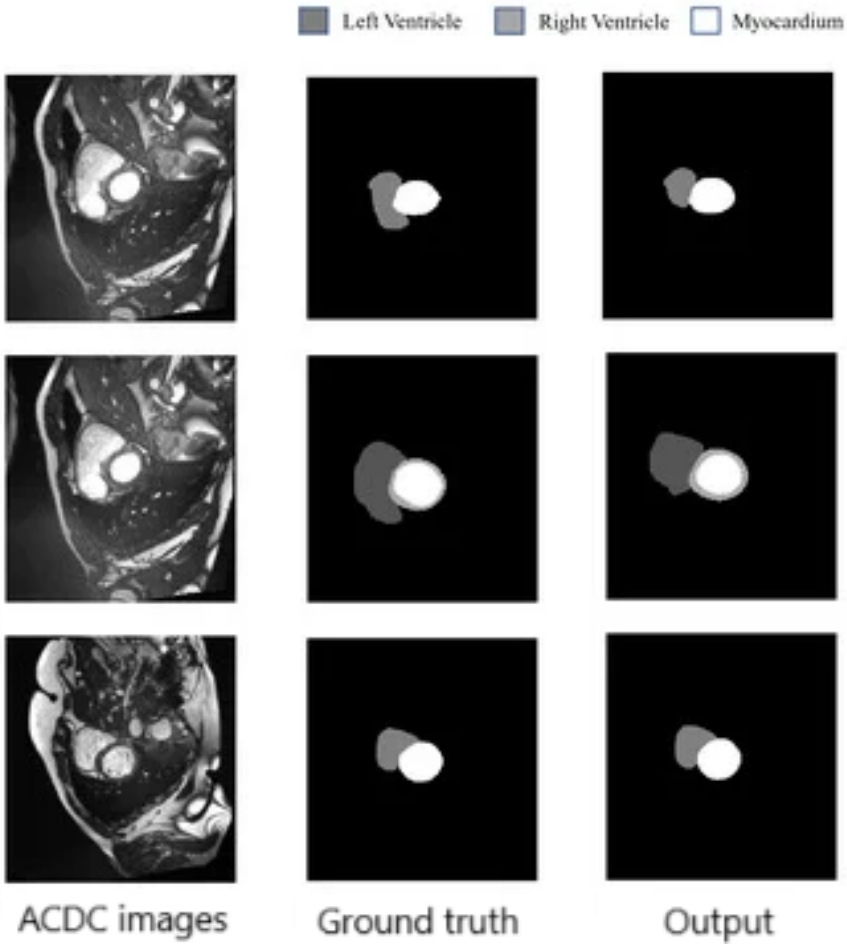



FIGURE 3.3. nnU-Net output example (adapted from [**47**])

As output, this network produces a set of segmented pictures that identify certain structures or regions of interest within the input medical images as we can see in Figure 3.3. In this case, we have a set of images very similar to the masks used in the training of the model which represent the left ventricle segmented region. The labeled output pictures effectively emphasizing the regions of interest based on the learnt patterns from the training data. These markers function as a segmentation map, assisting in the identification and localization of anatomical features or anomalies in medical pictures.

nnU-Net can work with 2D and 3D pictures with varying input modalities/channels. It is capable of comprehending voxel spacings and anisotropies, and it is resilient even when classes are very unbalanced. The number of training instances required for this network varies greatly depending on the complexity of the segmentation task and there is no such thing as a one-size-fits-all number. This network requires fewer training instances than other methods and it also allows us to carry out a training based on k-fold cross-validation technique. This process involves splitting the available medical imaging dataset into numerous folders, training the neural network on a mix of these subsets, and repeatedly validating on the remaining sections. Cross-validation reduces overfitting and offers a

more trustworthy assessment of the model's generalization performance across varied data subsets, confirming the network's success in segmenting unseen medical pictures.

Given a new dataset, nnU-Net will systematically analyze the provided training cases and create a 'dataset fingerprint'. Then it creates several U-Net configurations for each dataset:

- *2d*: a 2D U-Net (for 2D and 3D datasets);
- *3d_fullres*: a 3D U-Net that operates on a high image resolution (for 3D datasets only);
- *3d_lowres* and *3d_cascade_fullres*: a 3D U-Net cascade where first a 3D U-Net operates on low resolution images and then a second high-resolution 3D U-Net refined the predictions of the former (for 3D datasets with large image sizes only).

The creators of nnU-Net trained it using the medical images present in the ACDC dataset and made it available for free, so we can use pre-trained weights for our case. Using that dataset, this network works with four labels: label 0 if the pixel is inserted outside the segmented region (background), 1 if the pixel is inserted in the right ventricular area (RV), 2 if the pixel is inserted in the myocardial region (MV) and 3 if we are faced with a situation where the pixel is located in the left ventricle region (LV).

Model evaluation entails determining the accuracy of segmentation predictions using the Dice coefficient metric. The high performance of nnU-Net is achieved not through a new network architecture, loss function, or training scheme, but by systematizing the complex process of manual method configuration, which was previously addressed either through time-consuming manual tuning or purely empirical approaches with practical limitations.

This nnU-Net is a new segmentation tool that can be applied to a wide range of biomedical imaging datasets without any user intervention, making it ideal for users who need access to semantic segmentation methods but lack the expertise, time, data, or computing resources to adapt existing solutions to their problem [**46**].

### 3.2.2. Active contours model

As we have seen, the nnU-net neural network is very effective, but there are some limitations to its results [**48**]. The first problem derives from edge granularity, which presents a dilemma in cardiac structures with smooth patterns. Extracting good outputs from fragmented rather than smooth borders presents heightened difficulty. Furthermore, due to its deep-learning nature, the system faces edge circumstances in which it creates segmentations that are not anatomically possible.

In response to these limits, we use a boundary enhancement layer composed of two active contours. These dynamic contours are especially designed to reduce boundaries into smoother shapes and reducing granularity without sacrificing accuracy considerably. Furthermore, this technique helps to alleviate the difficulty of anatomically implausible segmentations by requiring comprehensive segmentation of both the myocardium (MYO)

and left ventricle (LV) regions. This requirement guarantees that both structures are completely contained, allowing the active contours to compress to their respective forms properly.

The modeling approach is iterative, beginning with the determination of the appropriate number of points. Subsequent iterations will focus on improving the segmentation of the most complicated sections. Finally, settings for edge repulsion and brightness attraction will be fine-tuned to enhance accuracy. The efficacy of the augmentation will be evaluated by comparing the basic segmentation's dice score to the enhanced segmentation, ensuring that any discrepancies are kept to a minimum.

The active contours model used in this study was created using *Scikit-image*, a popular *Python* library which provides a flexible foundation for exact boundary delineation and refinement. This algorithm is made up of nine important parameters [**49**]:

- **snake -** represents the starting contour or curve, which evolves to accurately conform to the boundary of the object.
- **alpha -** controls the elasticity of the contour, where a higher value increases its flexibility, making easy deformation, whereas a lower value yields a more rigid contour.
- **beta -** dictates the contour's smoothness, which influences its resistance to bending or curving. Higher beta values produce smoother outlines, whilst lower values allow for more dramatic curves.
- **w_line -** manages the contour's propensity for areas of brightness. A positive number attracts the contour to brighter sections, whereas a negative value pulls the contour to darker regions in the image.
- **w_edge -** regulates the contour's repulsion toward edges and abrupt changes in the picture. A positive number brings the contour closer to the edges, whilst a negative value pushes the contour away from them.
- **gamma -** controls the time-stepping behavior during the optimization process, determining the size of each iteration's time step. Higher gamma values result in greater updates every iteration, potentially quickening convergence but also creating instability. In severe instances, this may result in contour collapse. Lower gamma values, on the other hand, result in smaller but more steady updates every iteration, making the optimization process smoother.
- **max_num_iter -** as the name implies, this parameter determines the maximum number of iterations that the algorithm should do;
- **convergence -** determines a halting criterion based on the change in contour between iterations. Once the change falls below this threshold level, the algorithm terminates.
- **boundary_condition -** dictates the contour's interaction with the image boundaries and it can have multiple values, offering a range of possible behaviors. 'periodic' to join the snake's two ends, creating a continuous loop. It is suitable

for situations in which the contour must wrap around the picture limits; 'fixed' where the contour's endpoints are fixed and cannot be moved. It is useful when the contour does not extend beyond certain limitations; 'free' allows the contour's endpoints to shift freely in response to the form of the item within the picture; 'fixed-free' or 'free-fixed' combine the last two behaviors for the two endpoints, allowing one to remain fixed while the other moves freely.

The model requires an initial form to serve as the foundation for the active contour segmentation procedure (*snake*). These forms then constrict towards the borders of the Left Ventricle (LV) and Myocardium (MYO), enhancing the overall output.

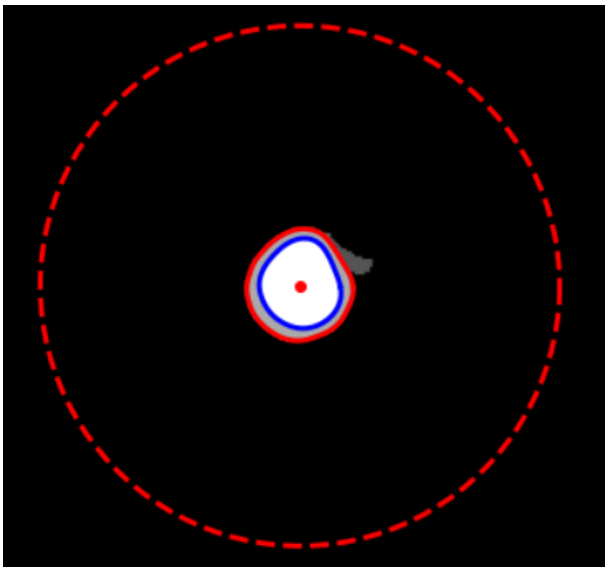


FIGURE 3.4. Active contour applied to both shapes (MYO and LV)

To obtain the contours illustrated in Figure 3.4, we have to first define the center of mass of the left ventricular segmentation performed earlier by the neural network. After completing these calculation, the attention moves to fine-tuning the shape's size and complexity, which is critical for the snake's performance and durability. The first form should incorporate a large circular arrangement, carefully planned to encircle every possible segmented zone.

The number of points along the MYO and LV contours must be carefully chosen to strike a delicate balance between efficiency and accuracy throughout the segmentation process. The appropriate number of points depends on a variety of criteria, including picture resolution, the complexity of the segmented form, and the segmentation objectives. Using fewer points results in a less exact depiction of the form, which frequently seems more round and stiff, leading to a faster segmentation. In contrast, using more points results in a more complex and flexible design with sharper edges. To determine the ideal number of points for the active contour method, we consider different sets of numbers of points, checking the impact of point density on the accuracy and efficiency of the segmentation process.

Similar to selecting the ideal number of points, the remaining initial parameters are chosen by repeated testing to maximize accuracy of this process.

### 3.3. Long-axis Segmentation

While short-axis images are routinely used to segment the LV due to their thorough cross-sectional representation, clinical interpretation sometimes necessitates seeing the LV in long-axis views, which give us a more comprehensive perspective of the heart's structure and function.

To achieve this, we used a method that includes recreating the LV geometry from the short-axis segmentation, which is commonly accomplished by interpolating and aligning the short-axis slices before reformatting them into long-axis views.

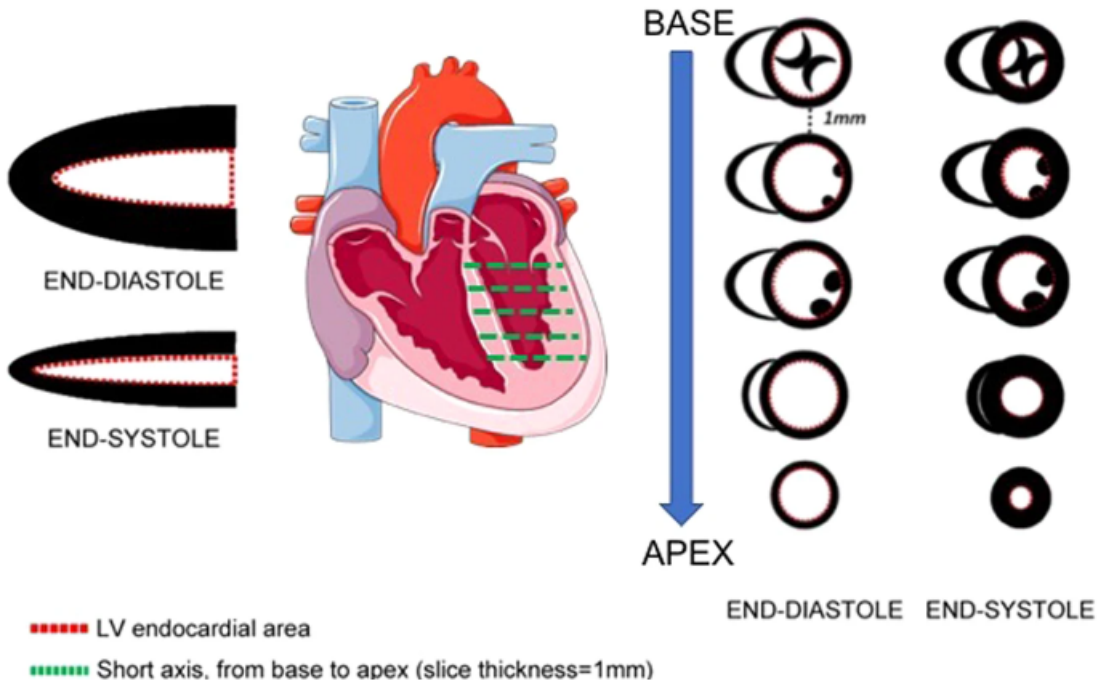



FIGURE 3.5. Left Ventricle long-axis reconstruction from short-axis slices (adapted from [**50**])

In the initial phase, we used the nnU-Net model's segmentation images obtained using the methodology explained in Subsection 3.2.1 of this chapter. To simplify the reconstruction procedure, each of the segmented images is split into ten different slices (2 basal slices, 6 mid slices and 2 apical slices). For each of the 10 slices (an example of how these slices are extracted can be seen in Figure 3.5), an active contours model, as detailed in the previous subsection was applied outlining the outside and inner limits (*snakes*) of the segmented left ventricular area. To perform the interpolation between short-axis and long-axis view, we needed to get the coordinates of the segmentation points and, for that, we created a custom function to properly identify corresponding points along inner and outer *snakes* of each slice. This function starts by retrieving the coordinates of the inner

and outer outlines. A tangent line is calculated for each point on the inner contour that is spaced at defined intervals. Then a perpendicular line to this tangent is then drawn and stretched to calculate the intersections with the outside contour. The intersection point that is closest to the inner contour is chosen as the equivalent outer point ensuring that only valid pairs, based on anatomical consistency, are selected. As the output of this function, we have the different pairs of inner and outer points.

The coordinates obtained before were used to recreate a vertical long-axis view of the left ventricle (also known as Apical 2-chamber view) in order to obtain a structure very similar to the one represented in the Figure 3.6. To reconstruct this structure, we first picked four critical points from each slice: two from the inner contour and two from the outside contour. These points were carefully chosen to reflect the borders of the left ventricle in each slice. Once these coordinates have been determined, we used them as initialization points for our active contours model, but this method does not directly link the initialization points. Instead, it uses those points to smoothly adapt and form a continuous and an anatomically correct border for the left ventricle. By combining all short-axis slices and applying active contours model we obtain a coherent and detailed vertical long-axis segmentation.

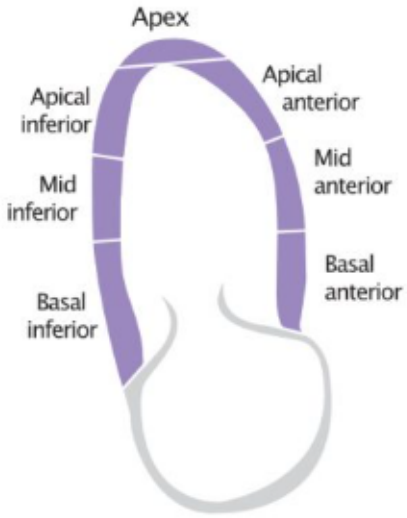



FIGURE 3.6. Vertical long-axis view (taken from [**51**])

Due to the capacity of *snakes* to adjust to the actual shape of the left ventricle, this entire reconstruction method approximates the left ventricle's vertical long-axis shape. While the approach captures the main shape of the left ventricle, it does not exactly recreate its anatomy due to the great difficulty of converting short-axis data into long-axis views. Despite these assumptions, the reconstructed image is sufficiently accurate for the computation of essential metrics, such as ventricular wall thickness.

CHAPTER 4

# Results and Discussion

In this chapter, we present the results and respective discussion about the methods introduced in the previous chapter. We follow the process from theory to practice, providing a full overview of how the strategies we picked materialized in our segmentation efforts.

This chapter describes the quantitative and qualitative outcomes of our segmentation algorithms, as well as a detailed assessment of their performance indicators. We investigate the complexities of the segmentation process, examining the influence of multiple factors and approaches on the accuracy and efficiency of segmentation outcomes. The discussion that follows digs into the relevance of these findings, establishing linkages to current literature.

## 4.1. Short-Axis results

The first process of obtaining results was the segmentation of the left ventricle, using the nnU-Net network and the ACDC dataset as an image database for neural network training and testing. Due to errors obtained when using the pre-trained network, it was necessary to retrain the model.

For this process, we used the following hardware: an Intel(R) Xeon(R) CPU E5-2660 0 @ 2.20GHz with a x86_64 architecture. It comprises 16 cores, each supporting 2 threads, resulting in a total of 32 threads. The clock speed is 2.20 GHz, with a maximum capability of 3.00 GHz. Noteworthy features include support for virtualization (VT-x) and the ability to execute both 32-bit and 64-bit instructions and the byte order is Little Endian. This processor was chosen due to its high processing capacity, which is necessary for image processing.

The first step of the segmentation process, using nnU-Net network, is to carry out a pre-processing method. This process involved the following sub-steps: image resampling to ensure that all input images have consistent spatial resolution; z-score normalization of the images to make them consistent across different frames and patients; data augmentation techniques, as random rotate data augmentation, to increase the model's robustness and ability to generalize and cropping the images to ensure that the masks resulting from segmentation are uniform to the ground truth representative masks. Once we have done all this pre-processing pipeline, we saved the pre-processed images and segmentation masks in a format compatible with nnU-Net, ensuring that the data is ready for training. Finally, we split the public dataset into training (80 %) and validation (20 %) which guarantees that the model is trained on one set of data and verified on another. The division of the training data of the model was done randomly using the cross folding

technique, where we have 5 folders (folder 0, 1, 2, 3 and 4), each containing 200 images (160 training images and 40 images for validation). Although we only have 100 patients for training, there are several patients that contain different frames, so we were able to obtain 200 images for training.

Once we have carried out this whole process, we then proceed to model training. As preliminary knowledge, through literature review, we know that the configuration that performs best on our data is *3d_fullres* (configuration explained in Subsection 3.2.1), so we trained the model with this configuration. For all 5 cross-validation folders, the model was trained using a batch size of 4, 1000 epochs, 250 iterations per epoch, 50 validation iterations per epoch, learning rate of 0.01, Robust Cross Entropy Loss as loss function and Stochastic Gradient Descent (SGD) as optimizer. Although all cross-validation folders had the same training parameters, the results obtained were different.

TABLE 4.1. Results obtained for each cross-validation folder

| **Folder** | **Training duration** | **Mean Validation Dice Score** |
|---|---|---|
| 0 | 363 929 seconds | 0.924 |
| 1 | 363 887 seconds | 0.922 |
| 2 | 365 532 seconds | 0.917 |
| 3 | 365 210 seconds | 0.923 |
| 4 | 364 174 seconds | 0.913 |

Table 4.1 shows us the main results obtained for each of the cross-validation folders. We can conclude that behavior between sets is fairly similar. Despite the neural network's complexity, we did not need to train it using 1000 epochs. We did it because it was the default value, and we only discovered it after a few days. The mean error evolution plot demonstrated that, after 250 epochs, the error remained constant. In order to have the general results of our model, we averaged the metrics of all training folders, achieving an average validation Score of 0.9198.

This result concern all patients, without any type of separation according to cardiac cycle phase or heart disease. In order to get a more detailed level of information, we obtained the segmentation accuracy metric for each pathological subgroup.

TABLE 4.2. Mean Dice Scores of the segmentation model for each pathological subgroup

| **Pathological Subgroup** | **Instance** | **Mean Dice Score** |
|---|---|---|
| Dilated Cardiomyopathy (DCM) | ED | 0.945 |
| | ES | 0.888 |
| | **Total** | 0.917 |
| Hypertrophic Cardiomyopathy (HCM) | ED | 0.942 |
| | ES | 0.894 |
| | **Total** | 0.918 |
| Myocardial Infarction (MINF) | ED | 0.947 |
| | ES | 0.902 |
| | **Total** | 0.925 |
| Healthy (NOR) | ED | 0.952 |
| | ES | 0.908 |
| | **Total** | **0.930** |
| Abnormal Right Ventricle (ARV) | ED | 0.932 |
| | ES | 0.873 |
| | **Total** | 0.903 |

According to results presented in Table 4.2, we can infer that there is a very similar behaviour in terms of accuracy among the different pathological subgroups. As expected, the Dice score results are greater during the End-Diastolic (ED) phase than the End-Systolic (ES) phase. During ED phase, the ventricle has a more uniform shape, and the border between the heart and surrounding tissues is clearer, allowing for more precise segmentation. In contrast, during ES phase, the ventricle contracts, resulting in a change of form and the borders between the heart and surrounding tissues may become less clear, posing obstacles for segmentation accuracy.

## 4.2. nnU-Net plus Active Contours results

As previously stated, the main goal of introducing the Active Contour model is to automatically and accurately trace the contour of the left ventricular segmentation output.

The first step was to determine the ideal number of points for the active contour method, where we considered different sets of numbers of points, checking the impact on the accuracy of the segmentation process. In addition to examining alternative numbers of points, we picked different test values for the *gamma* parameter (covered in subsection 3.2.2), which it is also very important. The model's accuracy results differ not only by these parameters, but also by the slice of the picture, therefore we validated segmentation across apex, mid, and basal slices which is critical for proper clinical interpretation. The best results of the tests performed can be seen in the tables 4.3 to 4.5.

TABLE 4.3. Results obtained for different parameters - Basal slice

| Number of Points | *Gamma* | Instance | Mean Dice Score | Best Dice Score |
|---|---|---|---|---|
| 100 | 0.005 | ED | **0.960** | **0.986** |
| | | ES | **0.812** | **0.985** |
| 100 | 0.0002 | ED | 0.943 | 0.970 |
| | | ES | 0.806 | 0.969 |
| 100 | 5e-05 | ED | 0.727 | 0.788 |
| | | ES | 0.721 | 0.955 |
| 500 | 0.005 | ED | 0.038 | 0.070 |
| | | ES | 0.025 | 0.049 |
| 500 | 0.0002 | ED | **0.952** | 0.966 |
| | | ES | **0.949** | **0.964** |
| 500 | 5e-05 | ED | 0.946 | **0.967** |
| | | ES | 0.909 | 0.946 |
| 1000 | 0.005 | ED | 0.035 | 0.070 |
| | | ES | 0.019 | 0.048 |
| 1000 | 0.0002 | ED | 0.347 | 0.451 |
| | | ES | 0.288 | 0.332 |
| 1000 | 5e-05 | ED | **0.944** | **0.961** |
| | | ES | **0.940** | **0.955** |

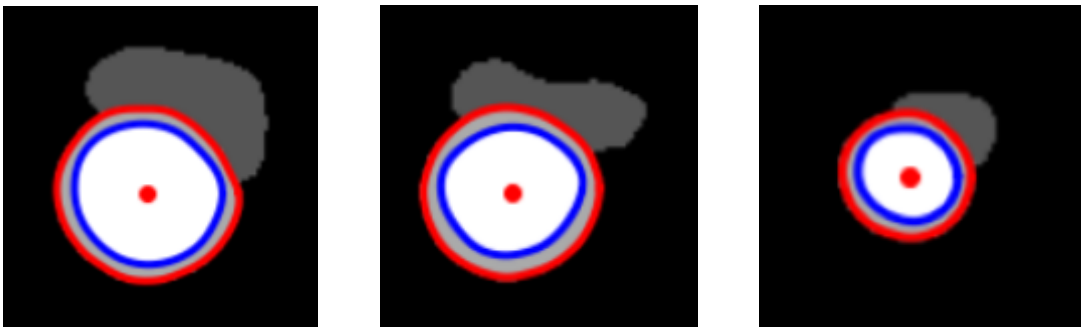
TABLE 4.4. Results obtained for different parameters - Mid slice

| Number of Points | *Gamma* | Instance | Mean Dice Score | Best Dice Score |
|---|---|---|---|---|
| 100 | 0.005 | ED | **0.973** | **0.991** |
| | | ES | **0.889** | **0.987** |
| 100 | 0.0002 | ED | 0.956 | 0.973 |
| | | ES | 0.878 | 0.975 |
| 100 | 5e-05 | ED | 0.736 | 0.945 |
| | | ES | 0.732 | 0.973 |
| 500 | 0.005 | ED | 0.044 | 0.067 |
| | | ES | 0.029 | 0.052 |
| 500 | 0.0002 | ED | 0.948 | 0.968 |
| | | ES | 0.942 | 0.958 |
| 500 | 5e-05 | ED | **0.957** | **0.971** |
| | | ES | **0.950** | **0.963** |
| 1000 | 0.005 | ED | 0.039 | 0.067 |
| | | ES | 0.022 | 0.052 |
| 1000 | 0.0002 | ED | 0.383 | 0.432 |
| | | ES | 0.304 | 0.350 |
| 1000 | 5e-05 | ED | **0.951** | **0.962** |
| | | ES | **0.942** | **0.957** |

TABLE 4.5. Results obtained for different parameters - Apical slice

| Number of Points | *Gamma* | Instance | Mean Dice Score | Best Dice Score |
|---|---|---|---|---|
| 100 | 0.005 | ED | **0.833** | **0.988** |
| | | ES | **0.737** | **0.981** |
| 100 | 0.0002 | ED | 0.795 | 0.908 |
| | | ES | 0.716 | 0.900 |
| 100 | 5e-05 | ED | 0.812 | 0.957 |
| | | ES | 0.722 | 0.924 |
| 500 | 0.005 | ED | 0.015 | 0.024 |
| | | ES | 0.007 | 0.019 |
| 500 | 0.0002 | ED | **0.828** | 0.934 |
| | | ES | **0.724** | **0.934** |
| 500 | 5e-05 | ED | 0.825 | **0.941** |
| | | ES | 0.709 | 0.895 |
| 1000 | 0.005 | ED | 0.014 | 0.024 |
| | | ES | 0.010 | 0.019 |
| 1000 | 0.0002 | ED | 0.156 | 0.173 |
| | | ES | 0.132 | 0.141 |
| 1000 | 5e-05 | ED | **0.821** | **0.930** |
| | | ES | **0.716** | **0.927** |

Although there are additional parameters, previously stated, in the design of the Active Contours model, we picked and tested just the most relevant and left the others as default values (*alpha*=0.01; *beta*=0.1; *w_line*=0; *w_edge*=1; *max_num_iter*=2500; *convergence*=0.1; *boundary_condition*='periodic'). There are variances in performance among basal, mid, and apical slices, but we can state that the basal slice has higher Dice scores than the mid and apical slices across several parameter combinations. The disparities in Dice scores between the ED and ES phases reflect the greater difficulty in making segmentation during ES phase, as reported previously, than the relatively stable ED period.



Basal Mid Apical

FIGURE 4.1. Active contours results for each slice

Reviewing all tests we can conclude that the set of parameters (100 points and *gamma*=0.005) led to the best outcomes of segmentation accuracy. In order to understand the disparities in shape across each test done, we can view the contours of different slices

obtained for the same patient example. These results show a lower Dice score for the apical slice, because it is smaller and more irregular in shape than basal and mid slices (also it can be seen in Figure 4.1).

This active contours technique was implemented to improve the segmentation outcomes of a simple nnU-Net network. To understand if the inclusion of this model would increase segmentation accuracy, we compared the mean segmentation performance of the nnU-Net alone vs the nnU-Net supplemented with the active contours model. The results obtained can be seen in Table 4.6.

TABLE 4.6. Mean segmentation performance of nnU-Net vs the nnU-Net plus active contours

| **Slice** | **Instance** | **Dice Score** | |
|---|---|---|---|
| | | **nnU-Net** | **nnU-Net + Contours** |
| Basal | ED | 0.952 | 0.960 |
| | ES | 0.825 | 0.812 |
| Mid | ED | 0.946 | 0.973 |
| | ES | 0.891 | 0.889 |
| Apical | ED | 0.807 | 0.833 |
| | ES | 0.780 | 0.737 |

Based on the results presented in the Table 4.6 and comparisons of the cardiac stages, we may conclude that the inclusion of dynamic contours is a success for the ED phase, because we have an increase in accuracy for every slice. As we know, left ventricle has a smaller area during the ES phase than it does during the ED phase. As a result, an inferior performance is totally acceptable at this instance, because the segmented region has a direct impact on the Dice score. Smaller areas typically result in lower Dice scores and the active contours model has more difficulties to correctly adapting to the left ventricle shape. In terms of slice results, we focus on the improvement of mid slice accuracy. The mean Dice score rises significantly indicating the efficiency of active contours in improving segmentation accuracy for this slice. For the remaining two slices, the models' overall results are very similar. The ED phase and Mid slice offer better results due to a clearer view of the left ventricle's morphology, but the ES phase and other slices produce lower accuracy since the left ventricle is less visible. Generally we can say that nnU-Net + Active Contours regularly outperforms nnU-Net alone.

### 4.3. Long-axis results

For this section, we used our private dataset since it has long-axis images, whereas the ACDC dataset only offers short-axis images. We applied the same method for our private dataset as we did for the ACDC dataset (an example can be seen in Figure 4.2). The images of our dataset were utilized as input for nnU-Net, which subsequently segmented the left ventricle. The segmentation output results were similar to those from the ACDC

dataset, suggesting a consistent performance of the neural network used across the two datasets. The only modification in this approach was that the private dataset included Digital Imaging and Communications in Medicine (DICOM) pictures, which required an extra step to convert them to NIFTI format before usage.

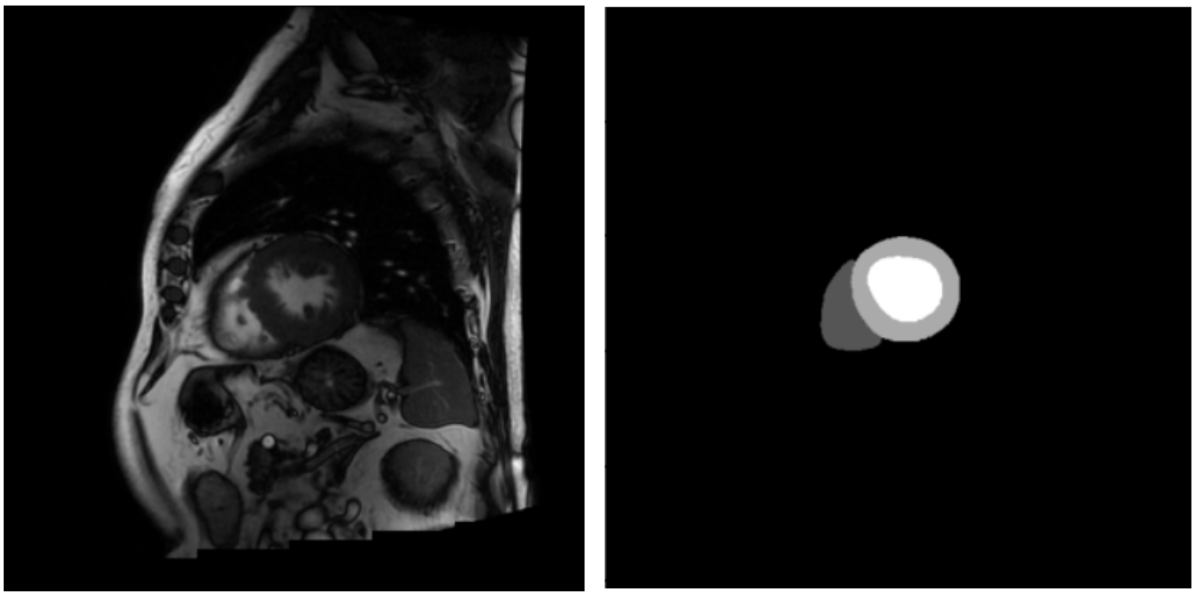


FIGURE 4.2. Private dataset short-axis image example (left) and its left ventricle segmentation output (right)

After completing the short-axis segmentation of the left ventricle, we proceeded with the long-axis reconstruction and segmentation.

### 4.3.1. Long-axis reconstruction

Starting with the segmentation results of the nnU-Net (example on the right of the Figure 4.2), we divided each image into ten different slices, with the first slice corresponding to the basal slice and the last to the apical slice.

For each of the ten slices, we applied our active contours model to accurately delineate the outer and inner boundaries of left ventricle in short-axis view where the results are very similar to those shown in the previous subsection. After we got the inner and outer *snakes* for each slice, we used our custom function (described in Section 3.3) which allows us to calculate the set of the different pairs of inner and outer points. For this calculation we used the minimum distance interval between coordinates in order to obtain as many points as possible. Once this process is done, we already have what is necessary to reconstruct the vertical long-axis view from the short-axis slices, so we started by choosing two pairs of points representing extremes of the left ventricle where each pair has the respective inner and outer points of the snake. By selecting these extreme coordinates and starting with apical slice points, we can create an estimated form for a long-axis left ventricle segmentation.

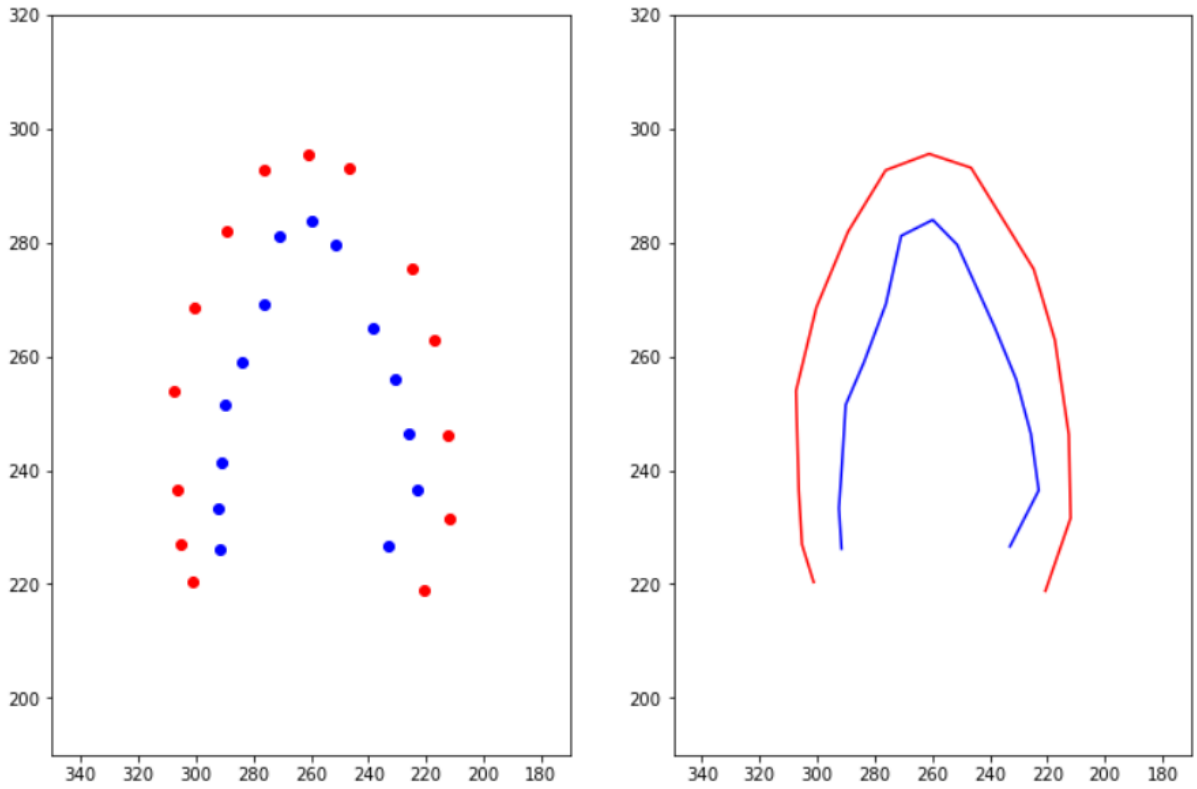



FIGURE 4.3. Baseline left ventricle reconstruction example

We pretended consistently obtain four essential points from each short-axis slice to precisely map the left ventricle anatomy. However, we had some problems with the apical slices, where the picture quality or distinctness of the ventricle borders were insufficient to properly apply the active contours model. In such circumstances, the points from these apical slices could not be used in the reconstruction, leaving small gaps between reconstruction points.

### 4.3.2. Long-axis segmentation

Connecting the extracted points from different slices (can be seen in the right part of Figure 4.3) was inadequate due to the complicated and curved morphology of the left ventricle structure so we had to use our active contours model to provide a more accurate estimate of the genuine shape of the left ventricle in the long-axis view.

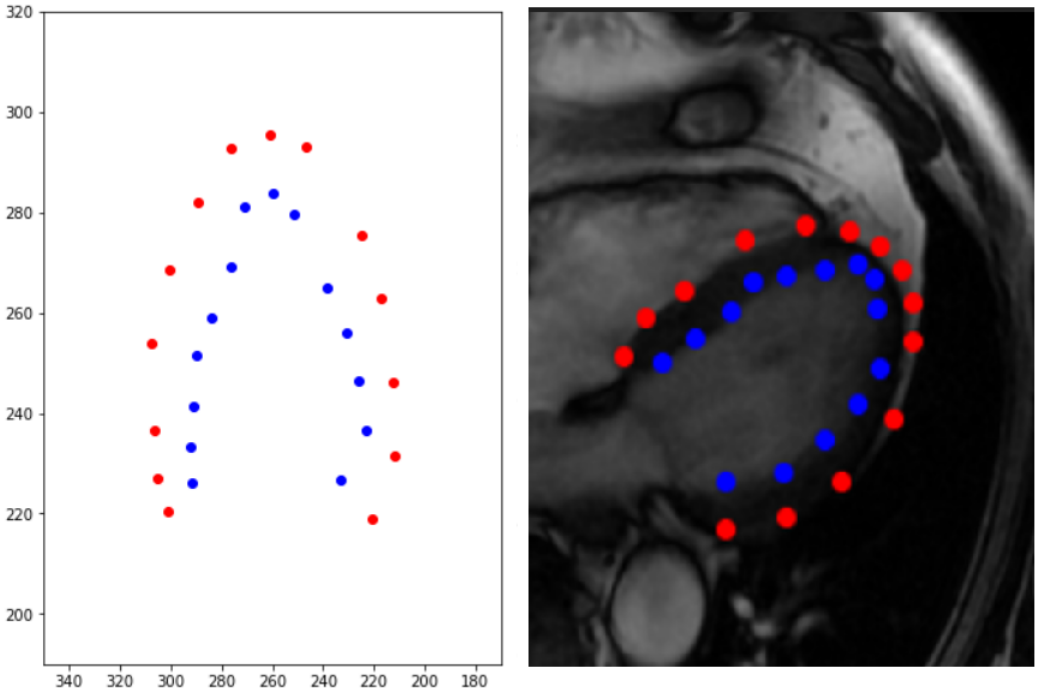



FIGURE 4.4. Reconstruction points overlaid on long-axis image

The first step was to ensure that reconstruction points, derived from several short-axis slices (Figure 4.4 left), precisely aligned with the left ventricle's location in a long-axis image. As we can see on the right side of Figure 4.4, when overlaying those points on the long-axis image, we can see that, while the fit is not perfect, it serves as a good starting point for a decent approximation of the left ventricle structure. It's important to note that we rotated the reconstruction points by 120 degrees to match them with the long-axis image.

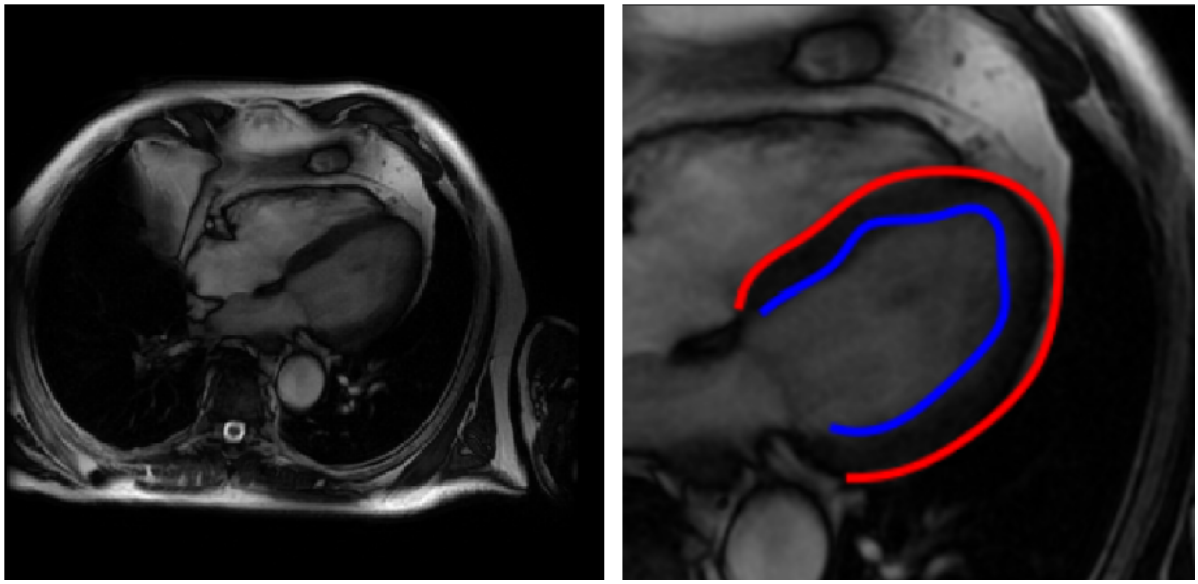


FIGURE 4.5. Active contours model results for long-axis segmentation

In the second stage, we used the reconstruction points as an initial boundary and employed the active contours model (*snakes*) to adjust the alignment with the left ventricle structure, as shown in Figure 4.5. The active contours model, starting with an approximation of the reconstruction points, give us a more precise segmentation that closely matches the true shape of the left ventricle in long-axis image. To ensure consistency with the original alignment, we rotated the *snakes* created in the same way we did with the reconstruction points.

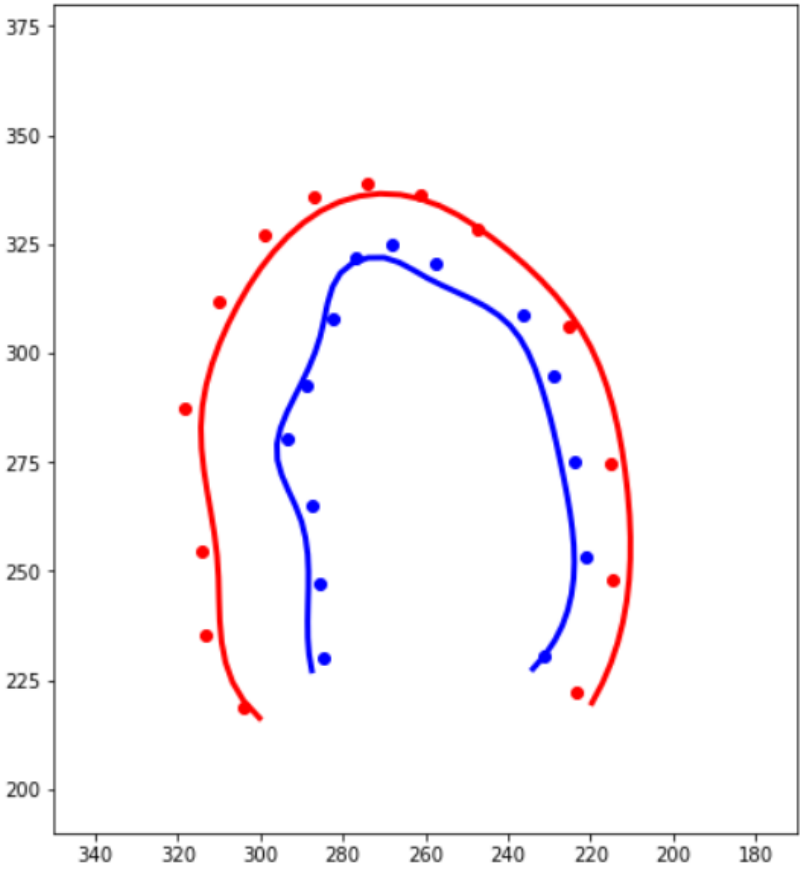



FIGURE 4.6. Long-axis reconstruction points and their active contours model results

In Figure 4.6 we can see the reconstruction points and *snakes* acquired from them during the segmentation process. It is critical to observe that the snakes do not perfectly align with the reconstruction coordinates. This difference occurs because the active contours model results adjust to the real anatomy of the left ventricle rather than merely following the starting reconstruction points.

The figures presented show that by combining data from different short-axis slices, we can obtain an almost precise long-axis reconstruction and segmentation of the left ventricle.

CHAPTER 5

# Conclusions

In this chapter, we review the important results and contributions of this research. We will explore the ramifications of our findings, their significance, and the limitations faced throughout the process. In addition, we propose areas for future work and research options to provide the groundwork for future research and innovation in this field.

## 5.1. Conclusion

Through this work, we proposed a pipeline that improves the accuracy of the left ventricle segmentation process by combining short-axis images with the active contours model and incorporating long-axis view.

First we used a nnU-Net network and the ACDC dataset as an image database for neural network training and testing. Due to errors when loading pre-trained network weights, it was necessary to retrain the model. Despite the innumerable amount of time it takes to train, this shows the enormous complexity and processing power of the network that can be proven by the fact that the nnU-Net network performed consistently and accurately across different cross-validation folders, with the mean validation Dice score averaging at 0.92. Regarding the pathological subgroups, we obtained a higher accuracy for normal patients (NOR) as expected, but the average dice scores of the other subgroups are not far from this one, so we consider it to be a success. The results demonstrated a greater accuracy during the ED phase compared to the ES phase, which is normal due to the ventricle's dynamic architecture during contraction.

To try to improve segmentation accuracy, we combined the Active Contours model with the nnU-Net output. The main objective of this combination was to improve the outlines of the left ventricle segmentation. The first set of tests were related to *snake* parameter tuning where the best results were obtained with 100 points and a gamma value of 0.005. Using these parameters for segmentation of the different slices, we conclude that basal slices had the best accuracy, followed by mid and apical slices. Regarding the cardiac phase, the active contours model integration considerably enhanced the accuracy of the ED phase while it produced mixed results for the ES phase. The overall results revealed that the nnU-Net with Active Contours model beat the standalone nnU-Net, showing that the pipeline adapts well to different conditions and may be able to aid in disease diagnosis.

Regarding long-axis left ventricle reconstruction and segmentation, although we had managed to get the coordinates of each short-axis slice to precisely map the left ventricle anatomy, we encountered issues with image quality and clarity of apical slices, forcing

small gaps between reconstruction points and prevented the complete capture of the LV's continuous shape. This can explain the small differences observed between the reconstruction points shape and the true long-axis ventricle structure (Figure 4.4). The use of our active contours model helped to adjust the alignment with the left ventricle structure, but as we can see from the figures presented in the previous chapter, the results are not perfect.

Even though there is potential for improvement, combining data from different short-axis slices produced a decent accurate long-axis segmentation of the left ventricle.

## 5.2. Future Work

The absence of large datasets is a significant barrier in medical imaging and cardiac analysis that should be addressed in future research. In general, the more data available, the more accurate the models, so if we want to obtain even better outcomes in this medical field, we need more data.

We also should testing some alternative values for the active contours model, as well as the development of an algorithm capable of automatically selecting the best parameters. In addition to choosing the optimal parameters, we should leverage the use of two snakes (one exterior and one inner) to improve segmentation. Both snakes should have the same structure, effectively "pushing" against each other while avoiding contact, resulting in a continual separation. This method can improve the accuracy of the segmentation process.

Based on long-axis shape of the left ventricle obtained with this work, an algorithm can be created to calculate metrics such as Global Longitudinal Strain (GLS) and Long-axis Strain (LAS), to compare the accuracy of reconstruction plus segmentation versus segmentation using only long-axis images.

We have only performed the long-axis reconstruction and segmentation process for one patient so we should expand this procedure to include additional patients and images, providing a more complete examination of the method's efficacy and robustness.

Future study should also consider using these presented work to develop a classification model capable of detect any potential heart illnesses.

# References


[1] Nichols M., Townsend N., Scarborough P., and Rayner M., "Cardiovascular disease in Europe: epidemiological update", *European Heart Journal*, vol. 37, pp. 3232-3245, nov. 2016.

[2] Frangi A. F., Niessen W. J., and Viergever M. A., "Three-dimensional modeling for functional analysis of cardiac images, a review", *IEEE Trans. Med. Imaging*, vol. 20, n.º 1, pp. 2-5, jan. 2001, doi:10.1109/42.906421.

[3] Kaus M., Berg J., Weese J., Niessen W., and Pekar V., "Automated segmentation of the left ventricle in cardiac MRI", *Medical Image Analysis*, vol. 8, n.º 3, pp. 245-254, sept. 2004, doi:10.1016/j.media.2004.06.015.

[4] Pednekar A., Kurkure U., Muthupillai R., Flamm S., and Kakadiaris I. A., "Automated Left Ventricular Segmentation in Cardiac MRI", *IEEE Trans. Biomed. Eng.*, vol. 53, n.º 7, pp. 1425-1428, july 2006, doi:10.1109/TBME.2006.873684.

[5] Radau P., Lu Y., Connelly K., Paul G., Dick A., Wright G., "Evaluation Framework for Algorithms Segmenting Short Axis Cardiac MRI", *The MIDAS Journal*, july 2009, doi:10.54294/g80ruo.

[6] Suinesiaputra, A. et al., "Left Ventricular Segmentation Challenge from Cardiac MRI: A Collation Study", *Statistical Atlases and Computational Models of the Heart. Imaging and Modelling Challenges*. vol. 7085, 2011.

[7] "Second Annual Data Science Bowl", https://www.kaggle.com/c/second-annual-data-science-bowl/overview. Accessed: 2023-03-02.

[8] Peffers K., Tuunanen T., Gengler C. E., Rossi M., and Hui W., "Design Science Research Process: A Model for Producing and Presenting Information Systems Research, *ArXiv*, 2020, doi:10.48550/ARXIV.2006.02763.

[9] "The Heart's Chambers", https://drramjimehrotra.com/the-hearts-chambers/. Accessed: 2023-03-02.

[10] Sheharyar, Ali et al., "Spatio-temporal Visualization of Regional Myocardial Velocities", *VCBM: Eurographics Workshop on Visual Computing for Biology and Medicine*, jan. 2016, doi:10.2312/vcbm.20161275.

[11] Ginat D.T., Fong M.W., Tuttle D.J., Hobbs S.K., Vyas R.C., "Cardiac imaging: Part 1, MR pulse sequences, imaging planes, and basic anatomy", *AJR Am J Roentgenol*, vol.197, pp.808-815, oct. 2011, doi: 10.2214/AJR.10.7231.

[12] Knipe H., Deng F., Hacking C., et al., "Cardiac imaging planes", *Radiopaedia.org*, doi: 10.53347/rID-43538.

[13] Luigi P. B., Marcelo H. M., Thor Edvardsen, et al., "European Association of Cardiovascular Imaging/Cardiovascular Imaging Department of the Brazilian Society of Cardiology recommendations for the use of cardiac imaging to assess and follow patients after heart transplantation ", *European Heart Journal - Cardiovascular Imaging*, vol. 16, pp.919-948, sept. 2015, doi: 10.1093/ehjci/jev139.

[14] Khened M., Kollerathu V. A., and Krishnamurthi G., "Fully convolutional multi-scale residual DenseNets for cardiac segmentation and automated cardiac diagnosis using ensemble of classifiers", *Medical Image Analysis*, vol. 51, pp. 21–45, jan. 2019, doi: 10.1016/j.media.2018.10.004.

[15] Abdelmaguid E. et al., "Left Ventricle Segmentation and Volume Estimation on Cardiac MRI using Deep Learning,", *arXiv*, 2018, doi: 10.48550/ARXIV.1809.06247.

[16] Brahim K., Arega T. W., Boucher A., Bricq S., Sakly, A., and Meriaudeau F., "An Improved 3D Deep Learning-Based Segmentation of Left Ventricular Myocardial Diseases from Delayed-Enhancement MRI with Inclusion and Classification Prior Information U-Net (ICPIU-Net),", *Sensors*, vol. 22, n.º 6, p. 2084, mar. 2022, doi: 10.3390/s22062084.

[17] Liao F., Chen X., Hu X., and Song S., "Estimation of the Volume of the Left Ventricle From MRI Images Using Deep Neural Networks,", *IEEE Trans. Cybern.*, vol. 49, n.º 2, pp. 495–504, feb. 2019, doi: 10.1109/TCYB.2017.2778799.

[18] Wu B., Fang Y., and Lai X., "Left ventricle automatic segmentation in cardiac MRI using a combined CNN and U-net approach,", *Computerized Medical Imaging and Graphics*, vol. 82, pp. 101-719, june 2020, doi: 10.1016/j.compmedimag.2020.101719.

[19] Clarysse P., "Evaluation of cardiac structure segmentation in cine magnetic resonance imaging", *Multi-Modality Cardiac Imaging: Processing and Analysis*, pp. 169–215, 2015.

[20] Bernard O. et al., "Deep Learning Techniques for Automatic MRI Cardiac Multi-Structures Segmentation and Diagnosis: Is the Problem Solved?", *IEEE Trans. Med. Imaging*, vol. 37, n.º 11, pp. 2514–2525, nov. 2018, doi: 10.1109/TMI.2018.2837502.

[21] Avendi M. R., Kheradvar A., and Jafarkhani H., "A combined deep-learning and deformable-model approach to fully automatic segmentation of the left ventricle in cardiac MRI ", *Medical Image Analysis*, vol. 30, pp. 108–119, may 2016, doi: 10.1016/j.media.2016.01.005.

[22] Tan L. K., Liew Y. M., Lim E., and McLaughlin R. A., "Cardiac left ventricle segmentation using convolutional neural network regression", *2016 IEEE EMBS Conference on Biomedical Engineering and Sciences (IECBES)*, pp. 490–493, dec. 2016, doi: 10.1109/IECBES.2016.7843499.

[23] Hesamian M. H., Jia W., He X., and Kennedy P., "Deep Learning Techniques for Medical Image Segmentation: Achievements and Challenges", *J Digit Imaging*, vol. 32, n.º 4, pp. 582–596, aug. 2019, doi: 10.1007/s10278-019-00227-x.

[24] Chen C. et al.,"Deep Learning for Cardiac Image Segmentation: A Review", *Front. Cardiovasc. Med.*, vol. 7, p. 25, mar. 2020, doi: 10.3389/fcvm.2020.00025.

[25] Hammouda K., Ng C. K., and El-Baz A.,"A New Framework for Performing Cardiac Strain Analysis from Cine MRI Imaging in Mice", *Scientific Reports*, vol. 10, p. 7725, may 2020, doi: 10.1038/s41598-020-64206-x.

[26] Wang Y. and Zhang W.,"A Dense RNN for Sequential Four-Chamber View Left Ventricle Wall Segmentation and Cardiac State Estimation", *Front. Bioeng. Biotechnol.*, vol. 9, p. 696227, aug. 2021, doi: 10.3389/fbioe.2021.696227.

[27] Xue W., Nachum I. B., Pandey S., Warrington J., Leung S., and Li S., "Direct Estimation of Regional Wall Thicknesses via Residual Recurrent Neural Network", *arXiv*, may 2017, doi: 10.48550/arXiv.1705.09728.

[28] Decourt C. and Duong L.,"Semi-supervised generative adversarial networks for the segmentation of the left ventricle in pediatric MRI", *Computers in Biology and Medicine*, vol. 123, p. 103884, aug. 2020, doi: 10.1016/j.compbiomed.2020.103884.

[29] Upendra R. R., Dangi S., and Linte C. A.,"An Adversarial Network Architecture Using 2D U-Net Models for Segmentation of Left Ventricle from Cine Cardiac MRI", *Functional Imaging and Modeling of the Heart*, vol. 11504, pp. 415–424, 2019, doi: 10.1007/978-3-030-21949-945.

[30] Isensee F., Jaeger P. F., Full P. M., Wolf I., Engelhardt S., and Maier-Hein K. H.,"Automatic Cardiac Disease Assessment on cine-MRI via Time-Series Segmentation and Domain Specific Features", *Statistical Atlases and Computational Models of the Heart. ACDC and MMWHS Challenges*, vol. 10663, pp. 120–129. doi: 10.1007/978-3-319-75541-013.

[31] Baumgartner C. F., Koch L. M., Pollefeys M., and Konukoglu E.,"An Exploration of 2D and 3D Deep Learning Techniques for Cardiac MR Image Segmentation ", *Statistical Atlases and Computational Models of the Heart. ACDC and MMWHS Challenges*, vol. 10663, pp. 111–119, 2018, doi: 10.1007/978-3-319-75541-012.

[32] Jang Y., Hong Y., Ha S., Kim S., and Chang H. J., "Automatic Segmentation of LV and RV in Cardiac MRI ", *Statistical Atlases and Computational Models of the Heart. ACDC and MMWHS Challenges*, vol. 10663, pp. 161–169, 2018, doi: 10.1007/978-3-319-75541-017.

[33] Zotti C., Luo Z., Lalande A., Humbert O., and Jodoin P. M.,"GridNet with automatic shape prior registration for automatic MRI cardiac segmentation", *arXiv*, sept. 2017, doi: 10.48550/arXiv.1705.08943.

[34] Khened M., Alex V., and Krishnamurthi G.,"Densely Connected Fully Convolutional Network for Short-Axis Cardiac Cine MR Image Segmentation and Heart Diagnosis Using Random Forest", *Statistical Atlases and Computational Models of the Heart. ACDC and MMWHS Challenges*, vol. 10663, pp. 140–151, 2018, doi: 10.1007/978-3-319-75541-015.

[35] Rohé M. M., Sermesant M., and Pennec X.,"Automatic Multi-Atlas Segmentation of Myocardium with SVF-Net ", *Cham: Statistical Atlases and Computational Models of the Heart. ACDC and MMWHS Challenges*, vol. 10663, 2018, doi: 10.1007/978-3-319-75541-0.

[36] Yang X., Bian C., Yu L., Ni D., and Heng P. A., "Class-Balanced Deep Neural Network for Automatic Ventricular Structure Segmentation ", *Statistical Atlases and Computational Models of the Heart. ACDC and MMWHS Challenges*, vol. 10663, pp. 152–160, 2018, doi: 10.1007/978-3-319-75541-016.

[37] Makowski P., Sørensen T. S., Therkildsen S. V., Materka A., Jørgensen H. S., Pedersen E. M.,"Two-phase active contour method for semiautomatic segmentation of the heart and blood vessels from MRI images for 3D visualization", *Computerized Medical Imaging and Graphics*, vol. 26, pp. 9-17, 2002, doi: 10.1016/S0895-6111(01)00026.

[38] Soomro S., Akram F., Munir A., Lee C. H., Choi K. N., "Segmentation of Left and Right Ventricles in Cardiac MRI Using Active Contours", *Comput Math Methods Med.*, 2017, doi: 10.1155/2017/8350680.

[39] Lankton S. and Tannenbaum A., "Localizing region-based active contours", *IEEE Transactions on Image Processing*, vol. 17, n.º 11, pp. 2029–2039, nov. 2008, doi: 10.1109/TIP.2008.2004611.

[40] Min H., Jia W., Wang X. F., et al., "An intensity-texture model based level set method for image segmentation", *Pattern Recognition*, vol. 48, n.º 4, pp. 1547–1562, 2015, doi: 10.1016/j.patcog.2014.10.018.

[41] Kawakubo M., Moriyama D., Yamasaki Y., Abe K., Hosokawa K., Moriyama T., Triadyaksa P., Wibowo A., Nagao M., Arai H., Nishimura H., Kadokami T., "Right ventricular strain and volume analyses through deep learning-based fully automatic segmentation based on radial long-axis reconstruction of short-axis cine magnetic resonance images", *MAGMA*, dec. 2022, doi: 10.1007/s10334-022-01017-3.

[42] Kalam K., Otahal P., Marwick T. H., "Prognostic implications of global LV dysfunction: a systematic review and meta-analysis of global longitudinal strain and ejection fraction", *Heart*, nov. 2014, doi: 10.1136/heartjnl-2014-305538.

[43] Afshin Farzaneh-Far, Romano S., "Measuring longitudinal left ventricular function and strain using cardiovascular magnetic resonance imaging", *European Heart Journal - Cardiovascular Imaging*, vol. 20, nov. 2019, pp. 1259–1261, doi: 10.1093/ehjci/jez097.

[44] "Neuroimaging Informatics Technology Initiative", https://nifti.nimh.nih.gov/. Accessed: 2023-10-20.

[45] "The Mayo Clinic", http://www.mayo.edu/bir/PDF/ANALYZE75.pdf. Accessed: 2023-10-20.

[46] Isensee, F., Jaeger, P. F., Kohl, S. A .A. et al., "nnU-Net: a self-configuring method for deep learning-based biomedical image segmentation", *Nat Methods 18*, pp. 203-211, 2021, doi: 10.1038/s41592-020-01008-z.

[47] Zhao, L., Zhou, D., Jin, X., Zhu, W., "nn-TransUNet: An Automatic Deep Learning Pipeline for Heart MRI Segmentation "*Life*, vol. 12, 2022, doi: 10.3390/life12101570.

[48] Schilling M., Unterberg C., Lotz J., Uecker M., "Assessment of deep learning segmentation for real-time free-breathing cardiac magnetic resonance imaging at rest and under exercise stress "*Scientific Reports*, vol. 14, 2024, doi: 10.1038/s41598-024-54164-z.

[49] Kass, M., Witkin, A., Terzopoulos, D., "Snakes: Active contour models ", *International Journal of Computer Vision 1*, vol. 321, 1988, doi: 10.1007/BF00133570.

[50] Russo, I., Micotti, E., Fumagalli, F. et al., "A novel echocardiographic method closely agrees with cardiac magnetic resonance in the assessment of left ventricular function in infarcted mice", *Sci Rep*, vol. 9, 2019, doi: 10.1038/s41598-019-40393-0.

[51] Edwards W. D., Tajik A. J., Seward J. B., "Standardized nomenclature and anatomic basis for regional tomographic analysis of the heart ", *Mayo Clin Proc*, vol. 56, pp. 479-497, 1981.